The Astrophysical Journal, 792:129 (22pp), 2014 September 10 doi:10.1088/0004-637X/792/2/129

THE CALIBRATION OF THE *WISE* W1 AND W2 TULLY–FISHER RELATION

J. D. Neill[1], Mark Seibert[2], R. Brent Tully[3], Hélène Courtois[4], Jenny G. Sorce[4,5], T. H. Jarrett[6], Victoria Scowcroft[2], and Frank J. Masci[7]
[1] California Institute of Technology, 1200 East California Boulevard, MC 278-17, Pasadena, CA 91125, USA
[2] The Observatories of the Carnegie Institute of Washington, 813 Santa Barbara Street, Pasadena, CA 91101, USA
[3] Institute for Astronomy, University of Hawaii, 2680 Woodlawn Drive, Honolulu, HI 96822, USA
[4] Institut de Physique Nucleaire, Université Claude Bernard Lyon I, F-69100 Lyon, France
[5] Leibniz-Institut für Astrophysik, D-14482 Potsdam, Germany
[6] University of Cape Town, Private Bag X3, Rondebosch 7701, Republic of South Africa
[7] Image Processing and Analysis Center (IPAC), California Institute of Technology, 1200 East California Boulevard, MC 100-22, Pasadena, CA 91125, USA
Received 2014 June 2; accepted 2014 July 21; published 2014 August 25

ABSTRACT

In order to explore local large-scale structures and velocity fields, accurate galaxy distance measures are needed. We now extend the well-tested recipe for calibrating the correlation between galaxy rotation rates and luminosities—capable of providing such distance measures—to the all-sky, space-based imaging data from the *Wide-field Infrared Survey Explorer* (*WISE*) W1 (3.4 μm) and W2 (4.6 μm) filters. We find a correlation of line width to absolute magnitude (known as the Tully–Fisher relation, TFR) of $\mathcal{M}_{W1}^{b,i,k,a} = -20.35 - 9.56(\log W_{mx}^{i} - 2.5)$ (0.54 mag rms) and $\mathcal{M}_{W2}^{b,i,k,a} = -19.76 - 9.74(\log W_{mx}^{i} - 2.5)$ (0.56 mag rms) from 310 galaxies in 13 clusters. We update the *I*-band TFR using a sample 9% larger than in Tully & Courtois. We derive $\mathcal{M}_{I}^{b,i,k} = -21.34 - 8.95(\log W_{mx}^{i} - 2.5)$ (0.46 mag rms). The *WISE* TFRs show evidence of curvature. Quadratic fits give $\mathcal{M}_{W1}^{b,i,k,a} = -20.48 - 8.36(\log W_{mx}^{i} - 2.5) + 3.60(\log W_{mx}^{i} - 2.5)^2$ (0.52 mag rms) and $\mathcal{M}_{W2}^{b,i,k,a} = -19.91 - 8.40(\log W_{mx}^{i} - 2.5) + 4.32(\log W_{mx}^{i} - 2.5)^2$ (0.55 mag rms). We apply an *I*-band −*WISE* color correction to lower the scatter and derive $\mathcal{M}_{C_{W1}} = -20.22 - 9.12(\log W_{mx}^{i} - 2.5)$ and $\mathcal{M}_{C_{W2}} = -19.63 - 9.11(\log W_{mx}^{i} - 2.5)$ (both 0.46 mag rms). Using our three independent TFRs (W1 curved, W2 curved, and *I* band), we calibrate the UNION2 Type Ia supernova sample distance scale and derive $H_0 = 74.4 \pm 1.4(\text{stat}) \pm 2.4(\text{sys})$ km s^{-1} Mpc^{-1} with 4% total error.

Key words: cosmological parameters – distance scale – galaxies: clusters: general – galaxies: distances and redshifts – galaxies: photometry – radio lines: galaxies

Online-only material: color figures, machine-readable table

1. INTRODUCTION

The utility of calibrating the power-law correlation between galaxy rotation rates and their luminosities (Tully & Fisher 1977) in the mid-infrared (MIR) has been clearly demonstrated by Sorce et al. (2013). Their use of the 3.6 μm *Spitzer* Infrared Array Camera (IRAC) photometry provided a calibration of the Tully–Fisher relation (TFR) with a scatter comparable to that seen in the *I* band (Tully & Courtois 2012). Having space-based photometry in the MIR mitigates the effects of dust and removes possible systematics when attempting to constrain the motions of galaxies across the entire sky.

While the IRAC 3.6 μm calibration is useful, there are a limited number of galaxies that have been observed through the camera's 4′ field of view. The W1 band of the *Wide-field Infrared Survey Explorer* (*WISE*, Wright et al. 2010) is similar in wavelength coverage ($\lambda_{\text{eff}} = 3.4\,\mu$m), is also space based, and thus enjoys all the benefits of the IRAC calibration. In addition, the *WISE* mission has covered the entire sky to a depth similar to the IRAC coverage of selected nearby galaxies. The number of calibrator galaxies with *WISE* imaging is 310, an increase of 46% over the sample available to Sorce et al. (2013), although the number of calibrator galaxies observed in the IRAC [3.6] band continues to increase. This additional utility of all-sky coverage motivated this work.

The *WISE* imaging represents the opportunity for providing high-quality 3.4 μm (W1) and 4.6 μm (W2) photometry over the entire sky; however, the automated catalog photometry available from the mission has not been optimized for extended galaxies. Corrections can be made to the catalog photometry; however, when applied to the TFR, the resulting scatter is significantly larger (0.69 mag, Lagattuta et al. 2013) than for the *I*-band calibration (0.41 mag, Tully & Courtois 2012). We have instigated a separate project to provide high-quality surface photometry of all *WISE* galaxies larger than 0.′8 on the sky. The *WISE* Nearby Galaxy Atlas (WNGA; M. Seibert et al., in preparation) will provide photometry that is quality controlled for over 20,000 galaxies. This photometry, optimized for extended sources, significantly reduces the resulting scatter in the TFR calibration and thus improves the resulting distances. Having an accurate calibration of the TFR for these two WISE passbands will allow the use of this large sample to explore the structure and dynamics of local galaxy bulk flows. This calibration has been completed and is presented herein.

The focus of this paper is the calibration of the TFR using photometry in the *WISE* W1 and W2 bands; however, we take the occasion to update the *I*-band calibration and present it in Section 4. We introduce a significant number of new calibration candidates by considering all galaxies associated with the calibrating clusters (see Section 2.1) contained in the Two Micron All Sky Survey (2MASS) redshift survey complete to $K = 11.75$ (Huchra et al. 2012).

Sorce et al. (2013) found a reduction in the scatter of the TFR when applying a correction to the IRAC photometry based on

the optical-MIR color with the optical measure being provided by *I*-band photometry. Unfortunately, there is no space-based all-sky survey in the *I* band. Thus, the uncorrected calibration for W1 and W2 may be useful for those wishing to extend their catalogs to as many galaxies as possible (those without *I*-band photometry), even though the scatter will be slightly larger. While the TFR in the optical has proven to be a straight power law, there is evidence that in the MIR there is curvature in the relation. We investigate that possibility and present our results in Section 5.

Once an accurate calibration is derived, we can use the distances derived thereby for calculating the Hubble constant, H_0 (Courtois & Tully 2012; Sorce et al. 2012b). We do this in Section 8.2 using the subset of clusters from the calibration set that have recession velocities that place them in the Hubble flow (>4000 km s^{-1}, Tully & Courtois 2012; Sorce et al. 2013). For a more robust measure of H_0 that extends well into the Hubble flow (to $z > 1$) we use TFR distances to renormalize the distance scale for the UNION2 Type Ia supernova (SN Ia) sample (Amanullah et al. 2010) and calculate H_0 directly from the renormalization in Section 8.3.

2. DATA

2.1. Calibrators

We adopt the galaxy cluster technique for deriving the calibration described by Tully & Courtois (2012) (see also Section 3.1). We take advantage of the fact that the galaxies within a given cluster are at the same distance and that the galaxy masses, and hence H I line widths, span a range large enough to determine the slope of the correlation for each cluster. We then shift each cluster along the luminosity axis such that their data appear to be from a single cluster. We iteratively combine the galaxy data derived from a set of 13 nearby clusters to derive a universal slope and then set the zero point of the relation using the universal slope applied to nearby galaxies with accurate distance measurements derived from independent techniques. To minimize the effect of the Malmquist bias, the slopes are derived from fitting the inverse Tully–Fisher relation (ITFR; Willick 1994). Details on the method and the calibrator and cluster sample can be found in Tully & Courtois (2012) and Sorce et al. (2013). The appendix in Tully & Courtois (2012) discusses issues specific to each of the 13 clusters.

In order to avoid excessive noise in the calibrations, we apply several cuts to the input sample (Tully & Courtois 2012). Because we must deproject the H I line widths based on the observed inclination, we exclude galaxies more face-on than 45°, the limit where typical errors in the deprojections begin to exceed 8%. Morphological types earlier than Sa greatly increase the scatter in the relation, most likely as a result of the mass of the bulge not contributing to the H I line width, and are excluded. Systems with insufficient or confused H I and galaxies that appear disrupted are also excluded. Following Sorce et al. (2013), the Tully & Courtois (2012) sample for A2634 has been extended to include the adjacent A2666, which is, within measurement uncertainties, at the same distance.

WISE photometry is available for all targets (see Table 1). The *Spitzer* photometry (Sorce et al. 2013) was acquired from pointed observations with the consequence that a significant fraction of calibration candidates remained unobserved (although the number observed continues to increase). Likewise, the *I*-band photometry, acquired by pointed observations, remains incomplete. With the current tally, there are 310 cluster calibrators with *WISE* W1 and W2 photometry, compared with 213 available to Sorce et al. (2013) for the *Spitzer* calibration, and 291 of the 310 *WISE* calibrators have *I*-band photometry, compared with the 267 available to Tully & Courtois (2012) for the previous *I*-band calibration.

A minor update with the current work is the conversion of Galactic obscuration values to Schlafly & Finkbeiner (2011) from Schlegel et al. (1998). This change has negligible impact on the *WISE* W1 magnitudes (and even less on W2) and only a 1%–2% impact at *I* band.

A small number of ambiguous cases are being rejected from the cluster calibration sample. One case is now not ambiguous: PGC 42081 was flagged in the earlier calibrations as possibly foreground to the Virgo Cluster. Recent *Hubble Space Telescope* observations provide a distance of 9.5 Mpc from a tip of the red giant branch (TRGB) measurement (Karachentsev et al. 2014), confirming that this galaxy is in the foreground. Further in the case of the Virgo Cluster, the galaxies PGC 41531 and PGC 43601 are considered probable background galaxies. Their velocities (1626 and 1783 km s^{-1} respectively) and distances are consistent with membership in the structure including the Virgo W Cluster and M Cloud at roughly twice the Virgo distance. Similarly, PGC 30498, which was considered as a candidate for the Antlia Cluster because of proximity on the sky, is now considered an outlying associate of the more distant Hydra Cluster. The velocity ranges of the two clusters overlap. PGC 30498, located between the two clusters, 3° from Antlia, has a velocity and distance compatible with Hydra. It is 5° from Hydra, too removed to be taken into the Hydra sample. See the Appendix of Tully & Courtois (2012) for discussions of the environments of these clusters.

The same inclination, morphology, and H I quality criteria described above are applied to our zero-point calibrator sample along with the additional constraint that each zero-point galaxy have a well-known distance derived from either Cepheid or TRGB measurements. To set the Cepheid distance scale, we use the recently updated LMC distance modulus of 18.48 ± 0.04 (Scowcroft et al. 2011, 2012; Monson et al. 2012; Freedman et al. 2012). We use a TRGB calibration that has been demonstrated to be consistent with the Cepheid scale by Rizzi et al. (2007) and Tully et al. (2008).

2.2. H I Line Widths

We use H I line width measurements from the Cosmic Flows project (Tully et al. 2013), which contains over 14,000 galaxies with measurements of W_{m50}, the width at 50% of the mean flux within the velocity range in the H I line that encompasses 90% of the total line flux. These data are available at the Extragalactic Distance Database (EDD) Web site.[8] This observed parameter is deprojected and corrected to a measurement of the intrinsic maximum rotation velocity width, W^i_{mx}. This is accomplished using a method that accounts for galaxy inclination, relativistic broadening, and finite spectral resolution as described in Courtois et al. (2009, 2011b) and reviewed in Tully & Courtois (2012). The error in W^i_{mx} is derived from the signal at the 50% level divided by the noise measured outside the line in regions of no signal. An error threshold of 20 km s^{-1} is applied to remove noisy measurements. Retained profiles meet a minimum per-channel signal-to-noise requirement of S/N $\geqslant$ 2 and are also visually inspected to remove pathological cases.

[8] http://edd.ifa.hawaii.edu; catalog "All Digital H I."

Table 1
Calibrator Data

PGC[a]	Name[b]	I_T[c]	$I_T^{b,i,k}$[d]	$W1_T$[e]	$W1_T^{b,i,k,a}$[f]	$W2_T$[g]	$W2_T^{b,i,k,a}$[h]	C_{I-W1}[i]	C_{I-W2}[j]	b/a[k]	Inc[l]	W_{mx}[m]	W^i_{mx}[n]	$\log(W^i_{mx})$[o]	Sam[p]
40095	NGC 4312	10.650 ± 0.152	10.230	11.252 ± 0.001	11.233	11.893 ± 0.001	11.899	−0.661	−1.327	0.27	79	217	221	2.344 ± 0.036	Virgo
40105	NGC 4313	10.537 ± 0.184	9.970	11.056 ± 0.001	11.028	11.653 ± 0.001	11.657	−0.716	−1.345	0.22	85	257	258	2.412 ± 0.028	Virgo
40201	NGC 4330	11.429 ± 0.189	10.810	11.936 ± 0.001	11.902	12.503 ± 0.001	12.503	−0.750	−1.351	0.17	90	251	251	2.400 ± 0.026	Virgo
40507	NGC 4380	10.109 ± 0.104	9.820	11.038 ± 0.001	11.043	11.651 ± 0.001	11.675	−0.881	−1.513	0.52	61	265	304	2.483 ± 0.042	Virgo
40516	NGC 4383	11.077 ± 0.088	10.870	11.603 ± 0.001	11.624	12.023 ± 0.002	12.060	−0.412	−0.848	0.58	56	199	239	2.379 ± 0.054	Virgo
40530	IC 3311	13.149 ± 0.107	12.810	13.964 ± 0.003	13.953	14.576 ± 0.007	14.587	−0.801	−1.435	0.21	86	160	160	2.205 ± 0.049	Virgo
40581	NGC 4388	9.973 ± 0.195	9.320	10.322 ± 0.001	10.291	10.571 ± 0.001	10.576	−0.629	−0.914	0.26	80	364	369	2.567 ± 0.024	Virgo
40622	NGC 4396	12.961 ± 0.126	12.670	12.449 ± 0.001	12.445	13.002 ± 0.003	13.017	0.567	−0.005	0.35	73	181	189	2.277 ± 0.045	Virgo
40644	NGC 4402	10.603 ± 0.154	10.170	10.763 ± 0.001	10.743	11.258 ± 0.001	11.264	−0.231	−0.752	0.34	74	267	278	2.444 ± 0.034	Virgo
40811	IC 3365	13.224 ± 0.080	13.060	14.462 ± 0.006	14.493	15.139 ± 0.016	15.184	−1.091	−1.782	0.42	68	122	132	2.120 ± 0.064	Virgo

Notes.
[a] Principal Galaxies Catalog (PGC) number.
[b] Common name.
[c] *I*-band mag (Vega mag).
[d] *I*-band mag with $A^I_{b,i,k}$ applied.
[e] *WISE* W1 magnitude (AB mag).
[f] W1 mag with $A^{W1}_{b,i,k,a}$ applied.
[g] *WISE* W2 magnitude (AB mag).
[h] W2 mag with $A^{W2}_{b,i,k,a}$ applied.
[i] $I_T^{b,i,k} - W1_T^{b,i,k,a}$ color (AB mag).
[j] $I_T^{b,i,k} - W2_T^{b,i,k,a}$ color (AB mag).
[k] Axial ratio b/a.
[l] Inclination in degrees.
[m] Uncorrected line width.
[n] Inclination-corrected line width.
[o] Logarithm of the inclination-corrected H I line width.
[p] Sample name.

(This table is available in its entirety in a machine-readable form in the online journal. A portion is shown here for guidance regarding its form and content.)

In subsequent plots, it becomes obvious that the errors in the H I line widths dominate the observational errors. Slow rotators exhibit a higher fractional error because of their small line widths. Lower inclination systems are also prone to higher errors, motivating our inclination threshold of 45°, below which a 5° error in inclination results in a >8% error in line width.

2.3. W1 and W2 Data and Photometry

Thanks to the *WISE* public data release, available from the NASA/IPAC infrared science archive (IRSA),[9] all of the galaxies in our sample have imaging in the *WISE* W1 and W2 bands. Image cutouts combining the level 1b (single) image products were drizzled using version 3.8.3 of the Image Co-addition with Optional Resolution Enhancement (ICORE) software (Masci & Fowler 2009; Masci 2013). To minimize background problems, we selected the 1b images with moon angles greater than 25°, and with epochs at least 2000 s from an annealing event. We combined the resulting image set on an output scale of $1\farcs0$ pixel^{-1}.

Photometry of the calibrator galaxies was performed using the photometry routines developed for the WNGA (M. Seibert et al., in preparation). This method uses elliptical apertures with fixed shapes, orientations, and centers but varying major axes in steps approximately equal to a resolution element in the W1 band ($6''$) to measure the flux of the galaxy within each annulus from the center to the edge of the galaxy. Foreground stars and contaminating neighbor galaxies are masked prior to measurement, and this masking is accounted for in computing the flux within each annulus. The influence of partially resolved and unresolved background galaxies is mitigated by allowing our sky value to contain flux from these objects. This is achieved by setting a masking limit in the sky annulus fainter than which objects are not masked. This produces an accurate sky that accounts for these fainter galaxies that will be present in the measurement annulus but are very difficult to detect and mask. Without this observed sky value, these faint, barely resolved galaxies prevent the surface photometry growth curve from converging.

The default axial ratios for the measurement ellipses for the WNGA are those given by HyperLEDA[10] (Paturel et al. 2003). However, since the dominant source of error in calibrating the TFR arises from errors in the H I line width inclination correction, much effort has gone into determining accurate axial ratios and from them inclinations. For this paper, we chose to use the axial ratios that were used to determine the correction to the H I line widths. These are derived from optical imaging, mostly *I* band (see Sections 2.4 and 4.4 in Courtois et al. 2011a). We found that, in the mean, the difference in the W1 photometry between using the default axial ratios and using the H I line width correction axial ratios was on the order of 4 mmag, well below our photometric error threshold.

In order to derive the total magnitudes of the galaxy in the *WISE* bands, $W1_T$ and $W2_T$, the radial photometric profile is analyzed and two versions of "total magnitude" are derived: (1) an asymptotic total magnitude that is the integration of the galaxy radial profile up to the point where the profile curve of growth has mathematically converged within the errors, and (2) a procedure that starts with the isophotal magnitude within 25.5 mag arcsec^{-2} and then adds a small extrapolation derived by extending an exponential disk fit to infinity (Tully et al. 1996). The extrapolation is given by the formula

$$\Delta m_{\rm ext} = 2.5 \log[1 - (1 + \Delta n)e^{-\Delta n}], \quad (1)$$

where $\Delta n = (\mu_{25.5} - \mu_0)/1.086$ is the number of disk exponential scale lengths between the central surface brightness μ_0 and the limiting isophotal surface brightness $\mu_{25.5}$. The exponential disk central surface brightness μ_0 excludes the bulge by defining the exponential disk fit over the range from the effective radius (enclosing half the light of the galaxy) to the $\mu_{25.5}$ isophotal radius. If the disk central surface brightness is brighter than $\mu_0 = 20$, then the correction $\Delta m_{\rm ext}$ is less than 0.03 mag.

The ensemble difference between these two types of magnitudes is characterized by a mean offset of 0.0003 mag and a standard deviation of 0.0234 mag. To check for a systematic trend with magnitude, we fit the differences as a function of asymptotic magnitude and derived a line with a slope of 0.0013 ± 0.0006 and a zero point of 0.0109 ± 0.0073. As a further check, we used both of these magnitudes to carry out the calibration, and the resulting set of coefficients were statistically identical. We have chosen to use the asymptotic magnitudes for the calibration presented herein because they are a standard output product of the WNGA and thus require no extra processing beyond our photometry pipeline. In addition, the extrapolated disk magnitudes are only appropriate for disk galaxies, while the asymptotic magnitudes are consistent regardless of galaxy type.

We convert our W1 and W2 magnitudes from the Vega to the AB system using the Vega-AB offsets of 2.699 mag for W1 and 3.339 mag for W2 from Table 3 of Section IV.4.h of the Explanatory Supplement to the *WISE* All-Sky Data Release Products.[11] Uncertainties in the observed W1 magnitudes are similar to or smaller than those measured for the IRAC [3.6] magnitudes (±0.05; Sorce et al. 2012a). The smaller uncertainties arise for galaxies that have a large number of individual images from the *WISE* survey and thus when coadded are deeper than the IRAC [3.6] images. This variable depth coverage in the *WISE* survey is due to the fact that the scans were conducted as great circles intersecting at the ecliptic poles (Wright et al. 2010), thus the frame coverage density increases from a minimum at the ecliptic plane to a maximum at the ecliptic poles.

We apply the following corrections to our measured total magnitudes:

1. $A_b^{[W1,2]}$, a Milky Way extinction correction (Schlafly & Finkbeiner 2011; Fitzpatrick 1999)
2. $A_i^{[W1,2]}$, an internal extinction correction (Giovanelli et al. 1995, 1997; Tully et al. 1998),
3. $A_k^{[W1,2]}$, a Doppler shift or *k*-correction (Oke & Sandage 1968; Huang et al. 2007).
4. $A_a^{[W1,2]}$, a total flux aperture correction from Table 5 of Section IV.4.c of the *WISE* Explanatory Supplement.[12]

In these and subsequent equations the notation $W1, 2$ means the values for the *WISE* W1 and W2 bands. All these corrections are discussed in detail in Sorce et al. (2012a). The internal extinction correction is described by the formula $A_i^{[W1,2]} = \gamma_{W1,2} \log(a/b)$ (Tully et al. 1998), where a/b is the

[9] http://irsa.ipac.caltech.edu/Missions/wise.html
[10] http://leda.univ-lyon1.fr
[11] http://wise2.ipac.caltech.edu/docs/release/allsky/expsup/sec4_4h.html
[12] http://wise2.ipac.caltech.edu/docs/release/allsky/expsup/sec4_4c.html

major-to-minor axial ratio and γ_{W1} has the form

$$\gamma_{W1} = 0.12 + 0.21\big(\log W^i_{mx} - 2.5\big). \quad (2)$$

The factor γ_{W2} can be obtained by multiplying γ_{W1} by the ratio of the reddening coefficients $R_{W2}/R_{W1} = 0.661$ (Fitzpatrick 1999). The k-corrections for $W1$ and $W2$ are very small and roughly the same over the redshift range of interest. The correction is based on Figure 6 in Huang et al. (2007) and has the form $A_k^{[W1,2]} = -2.27z$. The *WISE* aperture correction, $A_a^{[W1,2]}$, arises because the photometric calibration of *WISE* is conducted with point sources within a fixed aperture that misses some of the scattered light that is picked up in the extended apertures required to measure galaxies. The fixed apertures used for the *WISE* W1 and W2 photometric calibrations are 8.″25 in radius and therefore much smaller than any of the galaxies used in this paper; thus, each galaxy has fixed corrections of $A_a^{W1} = -0.034$ mag and $A_a^{W2} = -0.041$ mag applied. The fully corrected *WISE* magnitude is then

$$W1, 2_T^{b,i,k,a} = W1, 2_T - A_b^{[W1,2]} - A_i^{[W1,2]} - A_k^{[W1,2]} - A_a^{[W1,2]}. \quad (3)$$

2.4. I-band Photometry

The sources of the *I*-band photometry were discussed in Tully & Courtois (2012). There are contributions from Courtois et al. (2011a) and from the literature. The present calibration is augmented with 24 new galaxies, an increase of 9%. Photometric corrections and analysis procedures are the same as in the previous publication save for the small shift in reddening due to our Galaxy in going from Schlegel et al. (1998) to Schlafly & Finkbeiner (2011) and the small shift in distance scale zero point implicit in the shift of the LMC modulus from 18.50 to 18.48 (Scowcroft et al. 2011, 2012; Monson et al. 2012; Freedman et al. 2012).

The main interest of the current paper is the calibration of the *WISE* W1 and W2 band TFR, but an *I*-band recalibration is worth presenting. We collect *I*-band magnitudes because, as will be discussed in Section 6, we can couple the *I*-band and *WISE* magnitudes and recover the *I*-band scatter through an optical–*WISE* color correction. For determining the *WISE* color terms, we convert the *I*-band Vega magnitudes to the AB system using the offset from Frei & Gunn (1994) of 0.342 mag. This publication provides an opportunity to update the *I*-band calibration to assure consistency between optical and MIR distance measurements. For the *I*-band TFR recalibration, the native Vega system is used.

The resulting input data for calibrating the TFR are presented in Table 1. This table gives the input total W1 and W2 AB photometry, $W1_T$ and $W2_T$, the input total *I*-band Vega photometry, I_T, and the corrected magnitudes, $W1_T^{b,i,k,a}$, $W2_T^{b,i,k,a}$, and $I_T^{b,i,k}$, for each calibrator galaxy. Also presented are the optical to MIR AB colors, along with the axial ratios and inclinations, input and corrected H I line widths, and the sample (ZeroPt or cluster) each calibrator resides in.

3. THE W1 AND W2 CALIBRATION

The similarity of *WISE* W1 and W2 bands allows us to use identical procedures for both bands. Thus, we will describe both calibrations and present both sets of results together.

It has been shown that the Malmquist bias incurred by fitting the direct TFR can be mitigated by fitting the inverse relation (Willick 1994). The major effect of the bias in fitting the direct relation is to flatten the slope since fainter galaxies with the same line width are excluded by a photometric or signal-to-noise cut. Even with fitting the inverse relation, a residual bias due to scatter in the sample remains. This is addressed in Section 8.1.

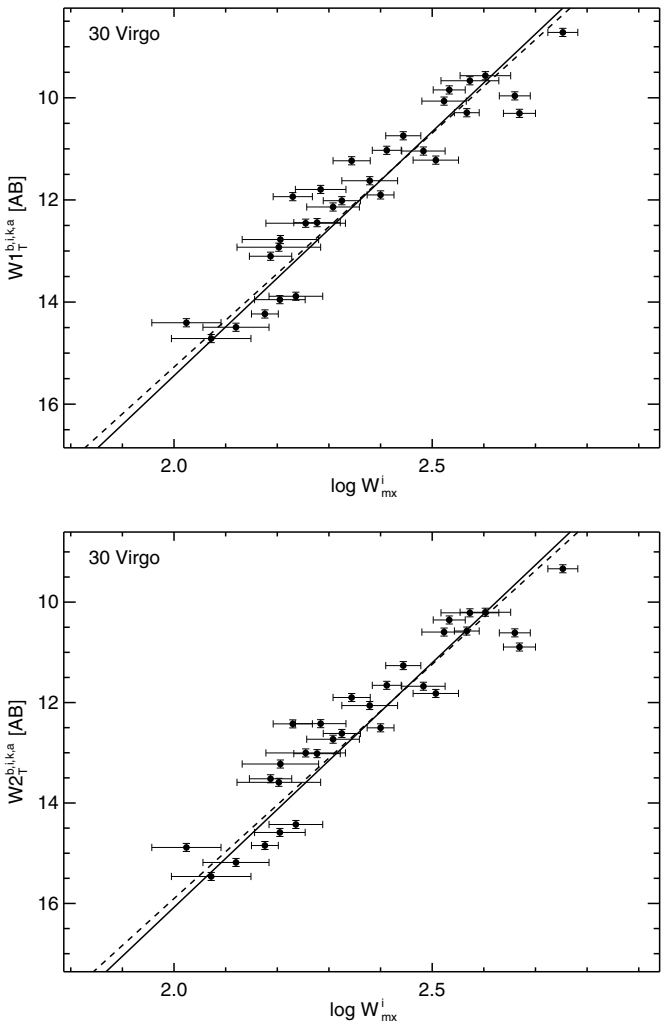

Figure 1. Linear TFR in the *WISE* W1 (top) and W2 (bottom) bands for the Virgo Cluster. The solid line is the inverse fit of the universal template correlation. The dashed line is the fit to Virgo alone.

We use a linear regression fitting technique that uses the line width errors as the input measurement error. For the *WISE* data, this is sensible since the formal measurement errors on the magnitudes are very small compared to the line width errors. The *I*-band magnitude errors are larger, and so we will make an adjustment to the line width errors that will account for these larger photometric errors (see Section 4).

3.1. Relative Distances and TFR Slope

The TFR posits a universal slope in luminosity versus H I line width. Our first step in deriving this universal slope is to fit each cluster individually. The results of these fits are shown in Figures 1 and 2. Examining the dashed lines in these figures shows how similar the individual slopes are. In addition, we see no significant trend in the slope with distance, a benefit of using the ITFR that mitigates the Malmquist bias. The slope values for the individual clusters are given in the third column of Tables 2 and 3.

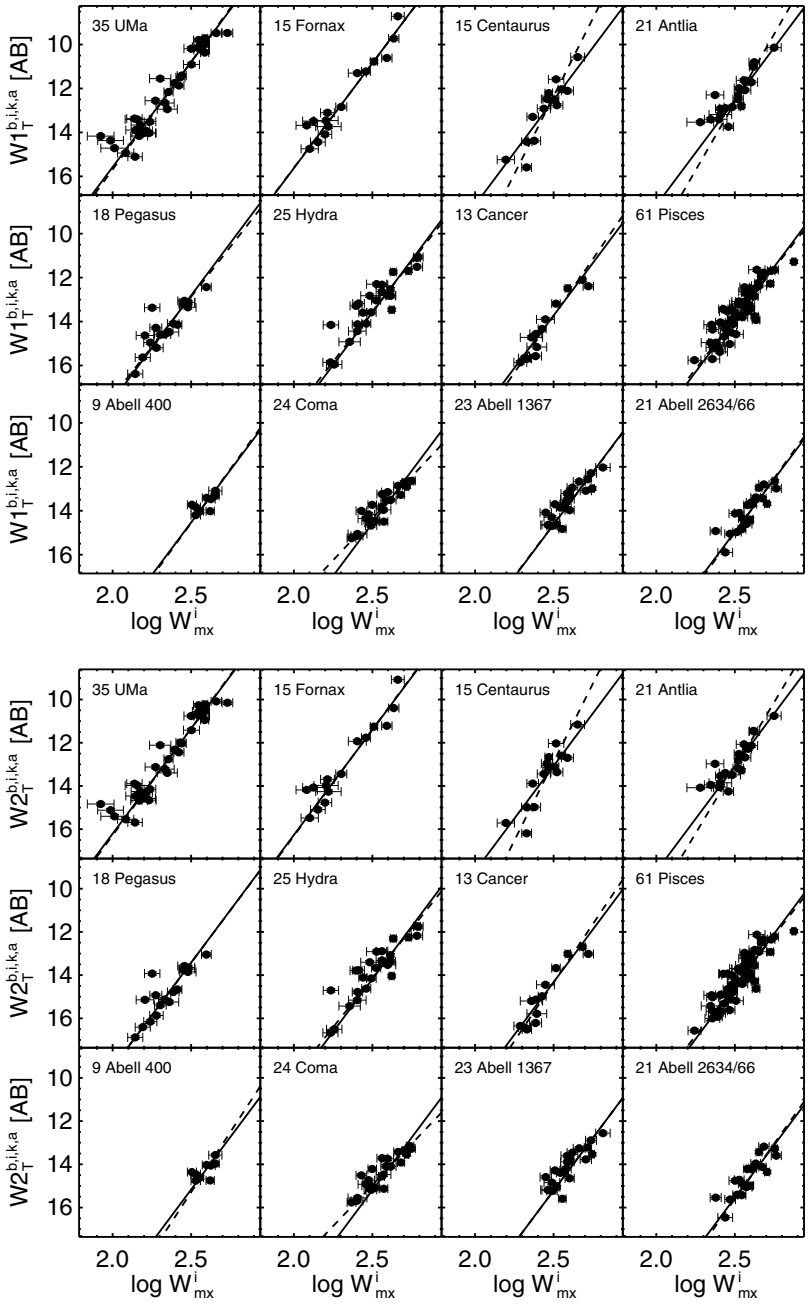

Figure 2. Linear TFR in the *WISE* W1 (top) and W2 (bottom) bands for Ursa Major, Fornax, Centaurus, Antlia, Pegasus, Hydra, Cancer, Pisces, A400, Coma, A1367, and A2634/2666. Solid lines are the inverse fit of the universal template, while dashed lines are the fits for each cluster.

In order to find the universal TFR, we must combine all 13 clusters by shifting the data along the magnitude axis, in effect moving each cluster to the same distance. Virgo is nearest and most complete and offers a natural choice for the reference cluster. The individual fits to each cluster provide an estimate of the relative distances from Virgo through comparing the TFR zero points (fourth column of Tables 2 and 3).

These zero points recommend the following groups. The first group is composed of Virgo, Ursa Major, and Fornax, a set that we consider the most complete because they are all nearby. This group is followed by the Centaurus–Antlia–Pegasus group, then the Hydra–Cancer–Pisces group, and finally the group composed of Coma and the three Abell clusters, A0400, A1367, and A2634/2666. As discussed in Tully & Courtois (2012) and Sorce et al. (2013), we adopt an iterative procedure for combining the clusters. Starting with the nearest group, we use the zero points for Fornax and Ursa Major to shift the galaxy magnitudes within those clusters to align with Virgo. A least-squares fit to the ITFR is then made to this aligned group. The resulting ensemble slope is then assumed in fitting all the individual clusters with only the zero points allowed to vary. Using these new zero points, we then shift the next group to align with Virgo and add it to the ensemble fit. This procedure is repeated, adding each of the groups in turn until we have a final ensemble fit for all 13 clusters. This procedure has been proven to work (Sorce et al. 2013; Tully & Courtois 2012) because the slope of the TFR is independent of the magnitude cutoff of each cluster.

Our resulting universal slopes are -9.56 ± 0.12 (W1) and -9.74 ± 0.12 (W2). The universal slopes and the shifted cluster

Table 2
W1 Cluster Fit Properties

Cluster[a]	N[b]	Slope[c]	ZP[d]	rms[e]	ZP_{cur}[f]	rms_{cur}[g]	N_{cc}[h]	ZP_{cc}[i]	rms_{cc}[j]
Virgo	30	-9.16 ± 0.38	10.66 ± 0.11	0.60	10.67 ± 0.06	0.55	30	10.83 ± 0.09	0.52
U Ma	35	-9.81 ± 0.37	10.80 ± 0.11	0.63	10.73 ± 0.05	0.70	34	10.95 ± 0.10	0.58
Fornax	15	-9.52 ± 0.56	10.85 ± 0.13	0.50	10.81 ± 0.09	0.53	15	10.99 ± 0.11	0.44
Antlia	21	-12.40 ± 1.30	12.54 ± 0.11	0.51	12.46 ± 0.05	0.50	16	12.70 ± 0.09	0.36
Centaurus	15	-14.16 ± 1.43	12.53 ± 0.15	0.59	12.49 ± 0.07	0.62	13	12.71 ± 0.14	0.52
Pegasus	18	-9.10 ± 0.81	12.81 ± 0.14	0.58	12.90 ± 0.09	0.57	17	13.00 ± 0.10	0.39
Hydra	25	-9.12 ± 0.43	13.59 ± 0.13	0.67	13.40 ± 0.04	0.57	19	13.74 ± 0.12	0.54
Pisces	61	-9.16 ± 0.28	13.91 ± 0.07	0.53	13.73 ± 0.03	0.50	59	13.93 ± 0.06	0.47
Cancer	13	-10.35 ± 0.63	13.73 ± 0.12	0.41	13.59 ± 0.06	0.41	13	13.80 ± 0.10	0.35
A400	9	-9.84 ± 2.67	14.54 ± 0.13	0.40	14.41 ± 0.07	0.34	8	14.67 ± 0.10	0.28
A1367	23	-9.46 ± 0.68	14.63 ± 0.09	0.46	14.43 ± 0.04	0.39	22	14.66 ± 0.09	0.42
Coma	24	-7.62 ± 0.40	14.58 ± 0.09	0.47	14.37 ± 0.04	0.36	24	14.60 ± 0.08	0.41
A2634/66	21	-9.91 ± 0.71	14.96 ± 0.10	0.48	14.73 ± 0.04	0.44	21	15.05 ± 0.09	0.43

Notes.
[a] Cluster name.
[b] Number of galaxies measured in cluster.
[c] Slope of the fit to individual clusters.
[d] Zero point with universal slope, no color correction (mag).
[e] Scatter about universal slope, no color correction (mag).
[f] Zero point with universal curve, no color correction (mag).
[g] Scatter about universal curve, no color correction (mag).
[h] Number of color-corrected galaxies measured in cluster.
[i] Zero point with universal slope after color correction (mag).
[j] Scatter about universal slope after color correction (mag).

Table 3
W2 Cluster Fit Properties

Cluster[a]	N[b]	Slope[c]	ZP[d]	rms[e]	ZP_{cur}[f]	rms_{cur}[g]	N_{cc}[h]	ZP_{cc}[i]	rms_{cc}[j]
Virgo	30	-9.33 ± 0.39	11.21 ± 0.12	0.64	11.21 ± 0.06	0.58	30	11.42 ± 0.10	0.52
U Ma	35	-9.90 ± 0.37	11.34 ± 0.11	0.63	11.27 ± 0.05	0.71	34	11.54 ± 0.10	0.57
Fornax	15	-9.85 ± 0.58	11.40 ± 0.14	0.56	11.34 ± 0.09	0.60	15	11.58 ± 0.12	0.45
Antlia	21	-12.13 ± 1.25	13.09 ± 0.11	0.51	13.00 ± 0.05	0.49	16	13.28 ± 0.09	0.35
Centaurus	15	-14.53 ± 1.49	13.08 ± 0.16	0.62	13.04 ± 0.07	0.65	13	13.30 ± 0.14	0.52
Pegasus	18	-9.70 ± 0.86	13.42 ± 0.14	0.61	13.50 ± 0.09	0.60	17	13.61 ± 0.09	0.38
Hydra	25	-9.13 ± 0.44	14.19 ± 0.14	0.70	13.97 ± 0.04	0.59	19	14.33 ± 0.12	0.55
Pisces	61	-9.28 ± 0.28	14.52 ± 0.07	0.54	14.32 ± 0.03	0.51	59	14.53 ± 0.06	0.47
Cancer	13	-10.84 ± 0.67	14.32 ± 0.13	0.48	14.16 ± 0.06	0.47	13	14.39 ± 0.10	0.37
A400	9	-11.14 ± 3.29	15.17 ± 0.14	0.43	15.03 ± 0.07	0.36	8	15.27 ± 0.10	0.29
A1367	23	-9.73 ± 0.72	15.22 ± 0.11	0.51	14.99 ± 0.04	0.43	22	15.24 ± 0.09	0.43
Coma	24	-7.61 ± 0.41	15.20 ± 0.11	0.52	14.97 ± 0.04	0.39	24	15.20 ± 0.09	0.42
A2634/66	21	-10.23 ± 0.76	15.55 ± 0.11	0.50	15.30 ± 0.04	0.45	21	15.64 ± 0.09	0.43

Notes.
[a] Cluster name.
[b] Number of galaxies measured in cluster.
[c] Slope of the fit to individual clusters.
[d] Zero point with universal slope, no color correction (mag).
[e] Scatter about universal slope, no color correction (mag).
[f] Zero point with universal curve, no color correction (mag).
[g] Scatter about universal curve, no color correction (mag).
[h] Number of color-corrected galaxies measured in cluster.
[i] Zero point with universal slope after color correction (mag).
[j] Scatter about universal slope after color correction (mag).

ensembles are shown in Figure 3, which is annotated with the zero-point offsets relative to Virgo for each cluster. The agreement in these offsets between the W1 and W2 data is quite good. The universal slope is also shown as the solid lines in Figures 1 and 2.

3.2. Zero Point and Absolute Distances

There are 37 nearby galaxies in our zero-point sample (see Table 1) that pass our selection criteria and for which there are good, independent distances from either the Cepheid period-luminosity method or the TRGB method. The distance moduli used are from Tully & Courtois (2012, Table 2). Since *WISE* is an all-sky data set, we are able to measure the total asymptotic W1 and W2 magnitudes for all of them and calibrate our distances in an absolute sense. We use the universal slope and the independent absolute magnitudes as input to our least-squares fit and allow only the zero point to vary. The resultant fits are shown in Figure 4.

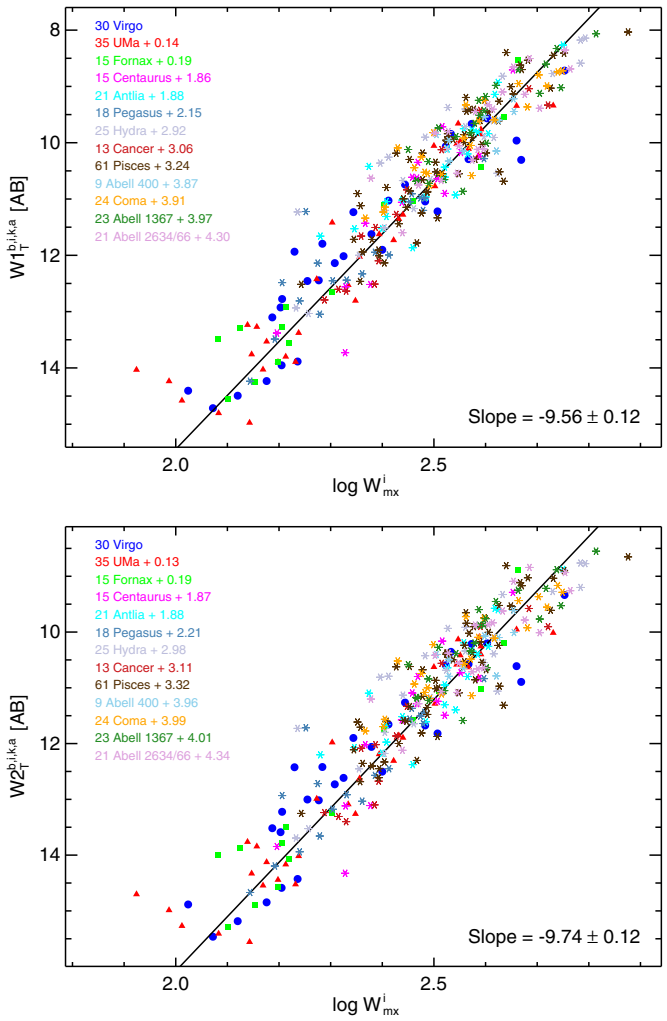

Figure 3. Linear TFR in the *WISE* W1 (top) and W2 (bottom) bands obtained from the galaxies in 13 clusters. Offsets given with respect to the Virgo Cluster represent distance modulus differences between each cluster and Virgo. The solid line is the least-squares fit to all of the offset shifted galaxies with errors entirely in line widths, the TFR. These relations have an rms scatter of 0.54 mag for W1 and 0.56 mag for W2.

(A color version of this figure is available in the online journal.)

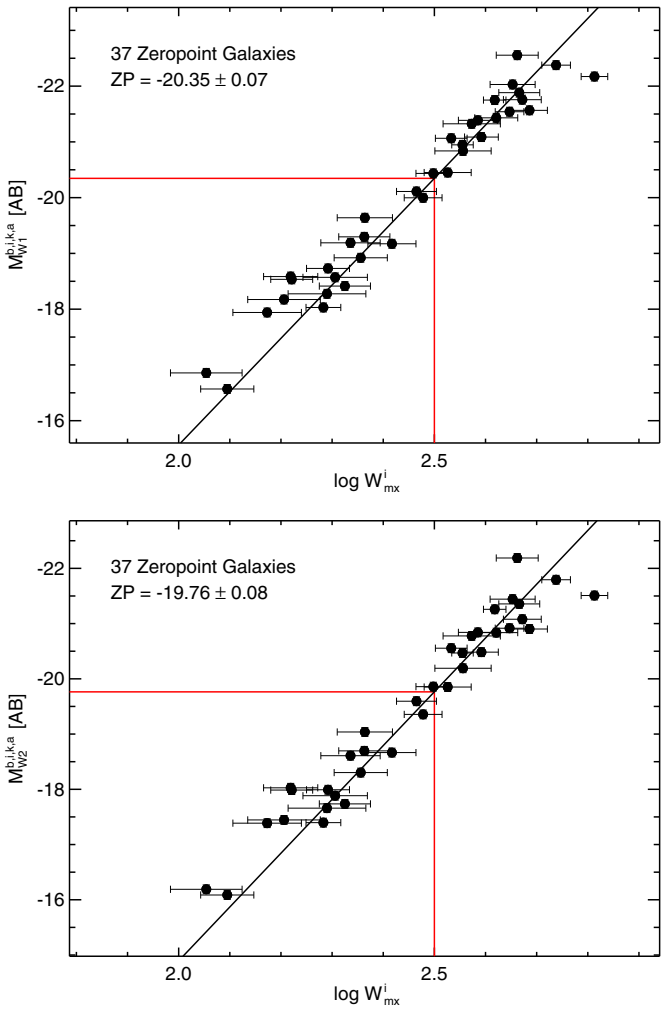

Figure 4. Linear TFR for the 37 galaxies with distances established by observations of Cepheid variables or the TRGB for the W1 (top) and the W2 (bottom). The solid black line is the least-squares fit with the slope established by the 13 cluster template. The zero point of the TFR is set at the value of this fit at $\log W^i_{mx} = 2.5$, as indicated by the solid (red) vertical and horizontal lines. The zero-point fits have an rms scatter of 0.45 mag for W1 and 0.49 mag for W2.

(A color version of this figure is available in the online journal.)

The measured zero points are -20.35 ± 0.07 for W1 and -19.76 ± 0.08 for W2. As was pointed out in Sorce et al. (2013), NGC 2841 is the fastest rotator and the biggest outlier. There is still no good reason to exclude this galaxy from the zero-point sample, so it is included here.

These zero points allow us to put the *WISE* TFR on an absolute scale. Since we have already calculated the cluster distances relative to Virgo, we need only calculate the offset between the constrained zero points in Figure 3 and the absolute zero points in Figure 4, apply these offsets to our W1 and W2 ensembles, and combine them with the zero-point calibrators, which we do in Figure 5. The zero-point calibration allows us to express the TFR as

$$\mathcal{M}^{b,i,k,a}_{W1} = -(20.35 \pm 0.07) - (9.56 \pm 0.12)\big(\log W^i_{mx} - 2.5\big), \quad (4a)$$

$$\mathcal{M}^{b,i,k,a}_{W2} = -(19.76 \pm 0.08) - (9.74 \pm 0.12)\big(\log W^i_{mx} - 2.5\big). \quad (4b)$$

We adopt a convention here and throughout the paper, that TFR predicted values are given in script; hence, our TFR predicted absolute magnitudes are given as $\mathcal{M}^{b,i,k,a}_{W1,2}$. To derive the distance modulus for a given galaxy based on pure W1 or W2 photometry, we subtract the appropriate predicted TFR absolute magnitude from Equation (4) from the input corrected total magnitude:

$$\mu_{W1,2} = W1, 2^{b,i,k,a}_T - \mathcal{M}^{b,i,k,a}_{W1,2}. \quad (5)$$

The rms scatter about the mean TFR will allow us to assess the usefulness of this relation for distance measurement. In order to do this, we use the zero point and the Virgo offset for each cluster to shift each galaxy magnitude in a given cluster onto the absolute magnitude scale. We compare this ensemble absolute magnitude, $M^{\rm ens}_{W1,2}$, with the predicted magnitudes from Equation (4) to derive the residual for every galaxy in the sample as follows:

$$\Delta M_{W1,2} = M^{\rm ens}_{W1,2} - \mathcal{M}^{b,i,k,a}_{W1,2}. \quad (6)$$

We calculate the rms scatter of the resulting ensemble of residuals. We define the scatter in this case to be the standard

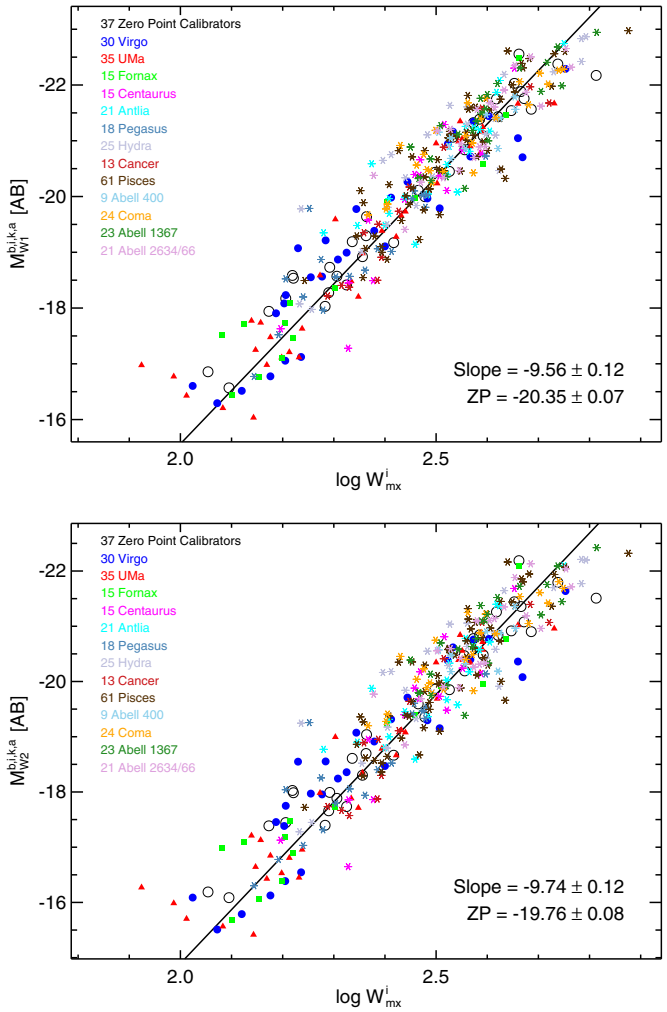

Figure 5. Linear TFR with slope fit to the galaxies in 13 clusters and the absolute magnitude scale set by 37 zero-point calibrators for the W1 (top) and the W2 (bottom).

(A color version of this figure is available in the online journal.)

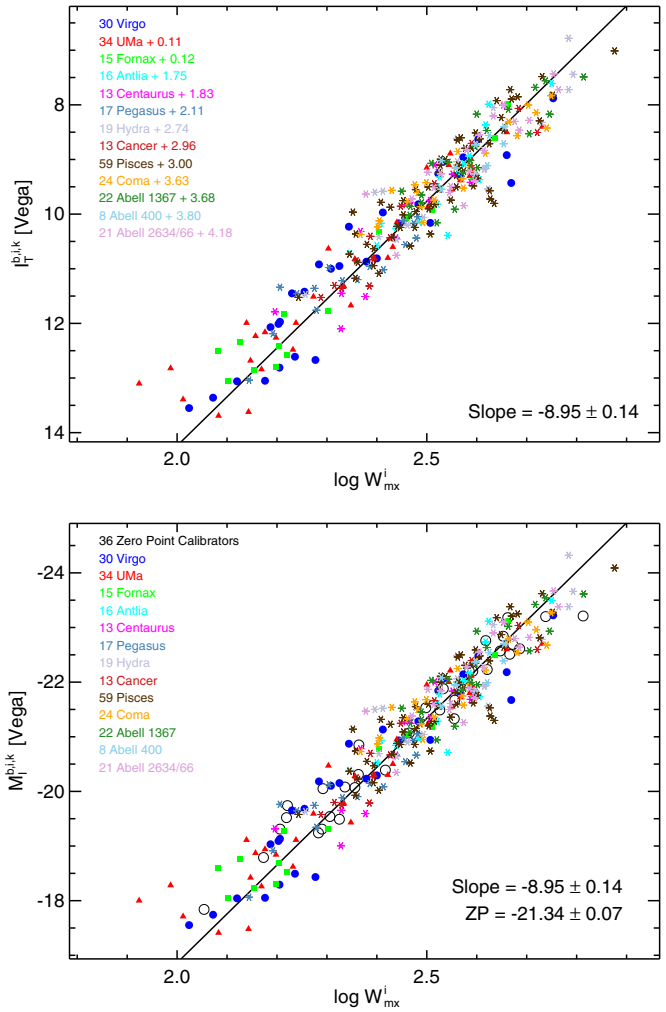

Figure 6. Linear TFR for *I* band (Vega) using galaxies shifted to the apparent distance of Virgo (top) and on the absolute magnitude scale set by 36 zero-point calibrators (bottom). This relation has an rms scatter of 0.46 mag and a zero-point rms scatter of 0.40 mag.

(A color version of this figure is available in the online journal.)

deviation of the residuals, or the square root of the second moment of the residuals. The distribution of the residuals is approximately Gaussian; therefore, one can take these values as a 1σ error, i.e., 68% of the galaxies fall within this 1σ envelope. The W1 calibration has a scatter of 0.54 mag, while the W2 calibration has a scatter of 0.56 mag, representing distance errors of 27% and 28%, respectively. The scatter in the zero-point fits is slightly better at 0.45 mag (W1) and 0.49 mag (W2). We point out that the formal errors on the zero-point values are much smaller at 0.07 mag (W1) and 0.08 mag (W2).

We expect the scatter in the W1 and W2 passbands to exceed that in the *I* band. Since, at a given line width, red and blue galaxies separate in magnitude in different passbands, the TFR rms scatter must change with passband. We expect the scatter in the TFR to reach a minimum where metallicity and young population effects are minimized. The empirical evidence suggests that the minimum is near the peak of the stellar light for disk galaxies around 1 μm. The *I* band is much closer to 1 μm than are the W1 and W2 bands.

Nonetheless, these are the pure *WISE* W1 and W2 TFRs requiring no other photometry to derive distance moduli to any galaxy. For a sample that may not have complete *I*-band coverage, one may decide that the statistical benefit of a larger sample outweighs the larger scatter of these pure *WISE* TFRs. Sorce et al. (2013) discuss the sources of this scatter in the MIR TFR and conclude that the most significant arises due to a color term in the TFR. We explore the analogous color terms for the *WISE* W1 and W2 data in Section 6. In addition, when comparing cluster distances derived from the pure *WISE* and the *I*-band TFRs, there is evidence for a systematic offset that may be the result of curvature in the pure MIR TFR. We discuss this in Section 5, but first we derive a new *I*-band TFR.

4. *I*-BAND CALIBRATION

We use the identical procedure to calibrate the *I*-band TFR as we did for the *WISE* calibration except we adjust the line width errors to account for the larger *I*-band photometric errors. This adjustment is carried out as follows. We use a preliminary TFR derived with the original line width errors to project the *I*-band photometric errors onto the line width axis. This generates a line width error due only to the photometric errors. This photometric line width error is then added in quadrature with the original line width errors, and the TFR is regenerated. The result of this final fitting is shown in Figure 6. The individual cluster fits and results for each of the calibration clusters are shown in Table 4.

Table 4
I-band Cluster Fit Properties

Cluster[a]	N[b]	Slope[c]	ZP[d]	rms[e]
Virgo	30	-8.75 ± 0.39	9.77 ± 0.09	0.51
U Ma	34	-8.46 ± 0.36	9.88 ± 0.10	0.57
Fornax	15	-8.64 ± 0.54	9.88 ± 0.11	0.42
Antlia	16	-11.26 ± 1.38	11.52 ± 0.10	0.40
Centaurus	13	-11.09 ± 1.22	11.60 ± 0.13	0.48
Pegasus	17	-7.54 ± 0.70	11.88 ± 0.10	0.43
Hydra	19	-9.03 ± 0.62	12.51 ± 0.13	0.55
Pisces	59	-9.63 ± 0.46	12.76 ± 0.06	0.46
Cancer	13	-8.85 ± 0.69	12.73 ± 0.09	0.32
A400	8	-9.58 ± 3.21	13.56 ± 0.10	0.28
A1367	22	-9.70 ± 0.93	13.45 ± 0.09	0.41
Coma	24	-7.00 ± 0.49	13.39 ± 0.08	0.39
A2634/66	21	-9.26 ± 0.83	13.94 ± 0.10	0.44

Notes.
[a] Cluster name.
[b] Number of galaxies measured in cluster.
[c] Slope of the fit to individual clusters.
[d] Zero point with universal slope (mag).
[e] Scatter about universal slope (mag).

The error adjustment flattens the TFR slightly from a slope of -8.97 to -8.95. The final TFR calibration from the *I*-band data can be expressed as

$$\mathcal{M}_I^{b,i,k} = -(21.34 \pm 0.07) - (8.95 \pm 0.14)\big(\log W_{mx}^i - 2.5\big). \quad (7)$$

The scatter is calculated in the same way as for the *WISE* calibration and results in a value of 0.46 mag rms, smaller than for the *WISE* bands as expected. The formula for the distance modulus using the *I*-band TFR is

$$\mu_I = I_T^{b,i,k} - \mathcal{M}_I^{b,i,k}. \quad (8)$$

The calibration cluster distances derived from the single-band uncorrected TFRs in the *WISE* bands and the *I* band are listed in the fifth through seventh columns of Table 5. The cluster distance offsets for the *WISE* linear TFR, relative to the *I*-band TFR, are illustrated by the (red) open diamonds in Figure 7. The particular cluster is indicated with the code listed in the second column of Table 5. We note that, compared to our *I*-band distances, the linear *WISE* TFR predicts distances that are lower for nearby clusters and higher for more distant clusters. If there is curvature in the MIR TFR, it could manifest itself in just this fashion (see Section V.a.i in Aaronson et al. 1986). Since we must use more distant clusters to estimate H_0 from the TFR, such a systematic deviation from a linear relation would bias the distances larger and produce a smaller H_0. Thus, it behooves us to consider this possible curvature in more detail.

5. CURVATURE IN THE MIR TFR

Curvature in the near-IR TFR has been seen before using *H*-band luminosities, as described in Aaronson et al. (1986, and references therein). We adopt the same strategy for dealing with the curvature, namely, we take an empirical approach rather than attempt to correct the magnitudes or line widths. Quadratic fits are also used in Sakai et al. (2000, Appendix C) for the $BVRIH_{-0.5}$ bands, which show an increase in the curvature term with wavelength.

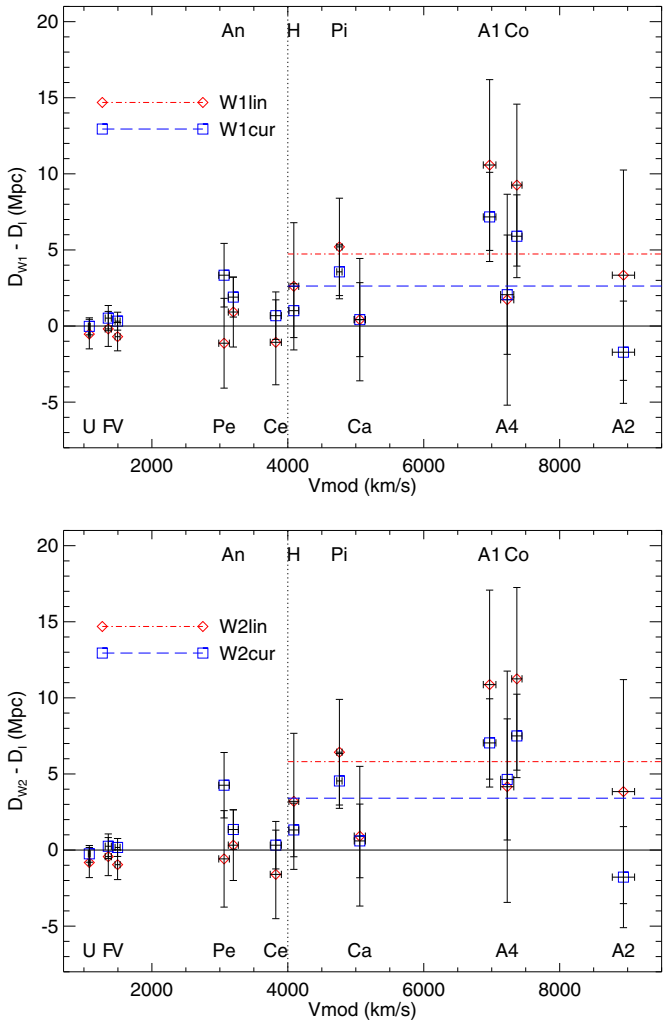

Figure 7. Distance offsets in Mpc relative to the *I*-band linear TFR of the calibration clusters for W1 (top) and W2 (bottom) using the linear TFR, shown by (red) diamonds, and the curved TFR, shown by (blue) squares. The dashed (blue) lines show the average offset for clusters beyond 50 Mpc (>4000 km s^{-1}) for the curved TFRs, while the dot-dashed (red) lines show the average offset for the linear TFRs.

(A color version of this figure is available in the online journal.)

We treat the curvature of the MIR TFR as an additional bias, or perturbation term on top of the linear relation seen in optical TFRs. By adding a curvature term, we are fitting the relation with a quadratic, and as such the curvature of a quadratic requires that we fit with the dependent variable in magnitudes. We attempted to fit an inverted quadratic, but the curvature does not follow the data well; thus, we are forced to fit the direct TFR. We minimize the Malmquist bias by using the ensemble of cluster galaxies shifted to the distance of Virgo with the linear TFR as the input for the fit. Fitting the direct relation with a least-squares fitter means that our errors will be on the magnitude axis; however, we have already stated that the line width errors dominate, especially compared to the *WISE* photometry. We therefore use the linear TFR to project the line width errors onto the magnitude axis and use these projected magnitude errors in the fitting.

We fit the same ensemble created from the linear fit to derive a universal curve. The results of these fits for both W1 and W2 are shown by the solid (green) lines in Figure 8, while the linear fits are shown by the dashed (red) lines (compare these to

Table 5
TFR Cluster Distance Comparison[a]

Cluster	Code	Tully & Courtois (2012)	Sorce et al. (2013)	This work						
				I Band	W1	W2	W1cur	W2cur	W1cc	W2cc
Virgo	V	15.9 ± 0.8	14.7 ± 0.9	16.6 ± 0.8	15.9 ± 0.9	15.6 ± 1.0	16.9 ± 0.6	16.8 ± 0.6	16.2 ± 0.8	16.2 ± 0.9
U Ma	U	17.4 ± 0.9	18.0 ± 0.9	17.5 ± 0.9	16.9 ± 1.0	16.6 ± 1.0	17.4 ± 0.6	17.2 ± 0.6	17.2 ± 0.9	17.1 ± 0.9
Fornax	F	17.3 ± 1.0	17.4 ± 1.2	17.5 ± 1.0	17.4 ± 1.2	17.1 ± 1.2	18.1 ± 0.8	17.8 ± 0.8	17.5 ± 1.0	17.4 ± 1.0
Antlia	An	37 ± 2	37 ± 2	38 ± 2	39 ± 2	38 ± 2	40 ± 1	39 ± 1	39 ± 2	39 ± 2
Centaurus	Ce	38 ± 3	39 ± 4	39 ± 3	38 ± 3	37 ± 3	39 ± 2	39 ± 2	39 ± 3	38 ± 3
Pegasus	Pe	43 ± 3	45 ± 3	44 ± 2	43 ± 3	43 ± 3	47 ± 2	48 ± 2	44 ± 2	44 ± 2
Hydra	H	59 ± 4	56 ± 4	59 ± 4	62 ± 4	62 ± 4	60 ± 2	60 ± 2	62 ± 4	62 ± 4
Pisces	Pi	64 ± 2	65 ± 3	67 ± 3	72 ± 3	73 ± 3	71 ± 2	71 ± 2	68 ± 3	68 ± 3
Cancer	Ca	65 ± 3	67 ± 4	66 ± 3	66 ± 4	67 ± 5	66 ± 2	66 ± 2	64 ± 3	64 ± 4
A400	A4	94 ± 5	97 ± 5	100 ± 5	102 ± 7	105 ± 8	103 ± 4	105 ± 4	100 ± 5	100 ± 6
A1367	A1	94 ± 5	96 ± 6	94 ± 5	104 ± 6	105 ± 6	101 ± 3	101 ± 3	98 ± 5	98 ± 5
Coma	Co	90 ± 4	95 ± 6	90 ± 4	99 ± 5	101 ± 6	96 ± 3	97 ± 3	94 ± 5	94 ± 5
A2634/66	A2	121 ± 7	112 ± 7	117 ± 6	121 ± 7	121 ± 7	116 ± 3	116 ± 3	117 ± 6	117 ± 6

Note. [a] All distances in Mpc.

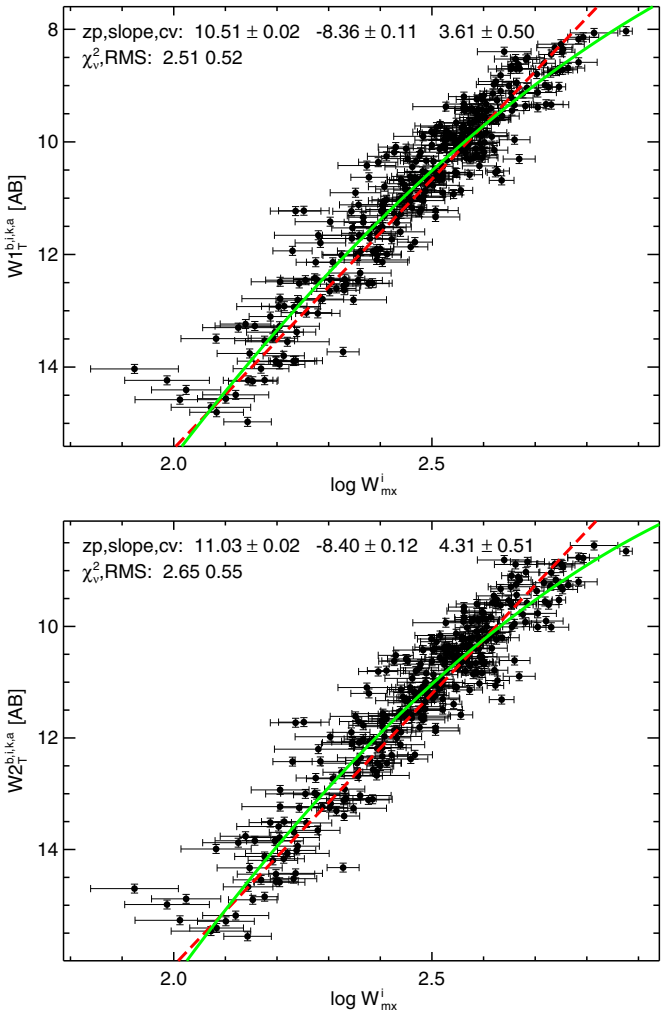

Figure 8. Fits to the ensemble of 13 clusters shifted to the distance of Virgo for the *WISE* W1 (top) and W2 (bottom). The solid (green) line is the quadratic error-weighted fit to the direct TFR with errors entirely in line width, projected onto the magnitude axis using the linear TFR. The dashed (red) line is the linear fit to the inverse TFR. The two fits are very similar, especially at the faint end. The annotations are for the curved direct fit and show an improvement in both rms scatter and χ^2_ν over the linear fit.

(A color version of this figure is available in the online journal.)

Figure 5 in Aaronson et al. 1986). We notice that the curved fits are close to the linear fits, especially at the faint end of the relations. The curved fits reduce the rms scatter from 0.54 to 0.52 mag in W1 and from 0.56 to 0.55 mag in W2. This brings the distance errors down to 26% in W1 and down to 27% in W2. In addition, the curved fits improve χ^2_ν, which goes from 3.1 to 2.5 in W1 and from 3.4 to 2.6 in W2.

We present the annotated ensemble in Figure 9 for W1 in the top panel and for W2 in the bottom panel. Both of the fits have similar slope terms of -8.36 ± 0.11 for W1 and -8.40 ± 0.12 for W2. The curvature terms are 3.60 ± 0.50 for W1 and 4.32 ± 0.51 for W2. We could compare these curvatures to the one found in Aaronson et al. (1986), for the *H* band; however, they use a different velocity measure for their TFR fitting. The distance modulus offsets from Virgo listed on the annotation for the figure are in reasonable agreement with those for the *I* band shown in Figure 6. The cluster distances shown in the fifth column of Table 5 for the *I* band are also in agreement with the distances for the curved *WISE* TFRs shown in the eighth and ninth columns. The distance offsets relative to the *I*-band TFR distances are shown graphically in Figure 7 by the (blue) open squares. It is clear that the curved fits reduce the systematic relative to the *I* band.

Now that we have a universal curve, we can use the same procedure that was used for the linear TFR to find the zero point of the curved relation. We present the results of the zero-point fitting in Figure 10. The formal errors on the zero-point values are smaller relative to the linear fits, as is the rms scatter, which is reduced from 0.45 to 0.39 mag in W1 and from 0.49 to 0.43 mag in W2. We point out that NGC 2841 is no longer such a large outlier as it was with the linear TFR. The final curved TFR is presented for both W1 and W2 in Figure 11. We express the curved *WISE* TFR as

$$\mathcal{M}^{b,i,k,a}_{W1} = -(20.48 \pm 0.05) - (8.36 \pm 0.11)\big(\log W^i_{mx} - 2.5\big) + (3.60 \pm 0.50)\big(\log W^i_{mx} - 2.5\big)^2, \quad (9a)$$

$$\mathcal{M}^{b,i,k,a}_{W2} = -(19.91 \pm 0.05) - (8.40 \pm 0.12)\big(\log W^i_{mx} - 2.5\big) + (4.32 \pm 0.51)\big(\log W^i_{mx} - 2.5\big)^2. \quad (9b)$$

The distance modulus can then be calculated as before with Equation (5).

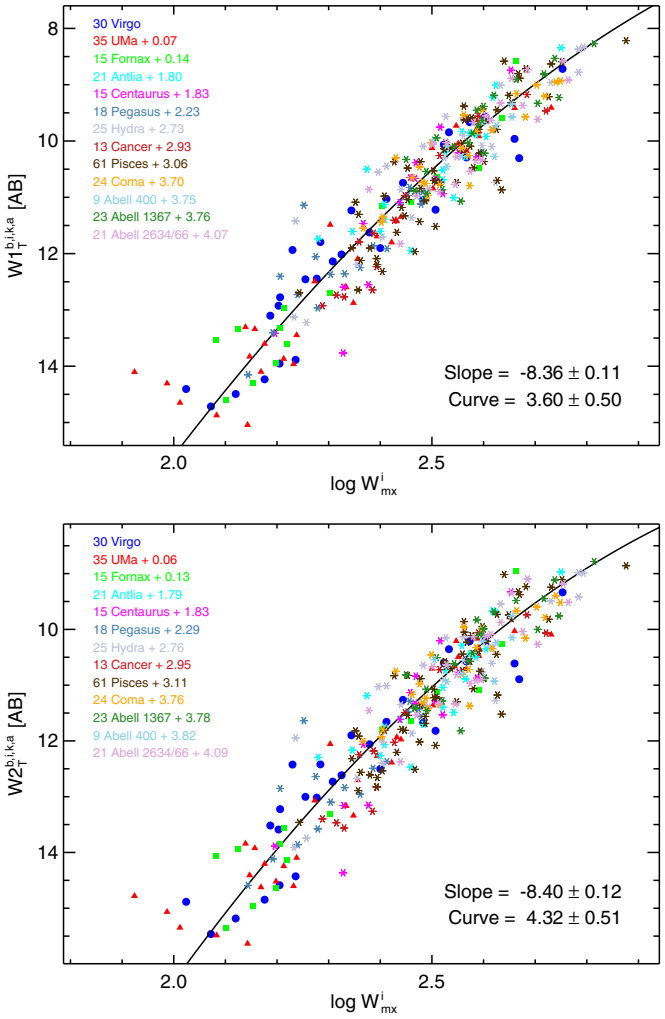

Figure 9. Curved TFR in the *WISE* W1 (top) and W2 (bottom) bands obtained from the galaxies in 13 clusters. Offsets given with respect to the Virgo Cluster represent distance modulus differences between each cluster and Virgo. The solid line is the least-squares fit to all of the offset-shifted galaxies with errors entirely in line widths, projected onto the magnitude axis using the linear TFR. The relations have an rms scatter of 0.52 mag for W1 and 0.55 mag for W2.

(A color version of this figure is available in the online journal.)

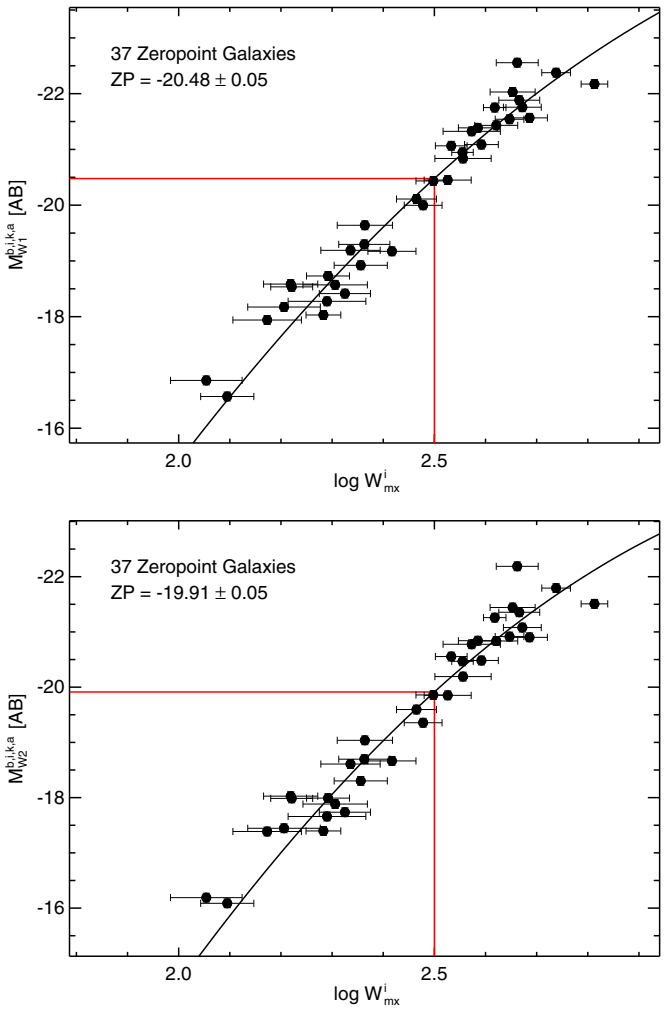

Figure 10. Curved TFR for the *WISE* W1 (top) and W2 (bottom) band using the 37 galaxies with distances established by observations of Cepheid variables or the TRGB. The solid line is the least-squares fit with the coefficients established by the 13 cluster template. The zero point of the TFR is set at the value of this fit at $\log W^i_{mx} = 2.5$ as indicated by the solid (red) vertical and horizontal lines. The zero-point fits have a scatter of 0.39 mag in W1 and 0.43 mag in W2.

(A color version of this figure is available in the online journal.)

6. OPTICAL–MIR COLOR TERM

We do not repeat the color term discussion from Sorce et al. (2013); however, we remind the reader that there is good reason to suspect that a color term might exist because the TFR steepens with wavelength. Indeed, such a color term was detected in Sorce et al. (2013) (see their Section 3.3 and their Figures 6–8) and was used to reduce their scatter from 0.49 to 0.44 mag. The *WISE* data also show correlations between the optical-to-MIR color and the mean linear TFR residuals as shown in Figure 12. Figure 13 shows an attempt to find a similar trend in the *I*-band residuals, but the slope of our fit is consistent with an insignificant (1.2σ) correlation. We note that in this section we are using the linear, not the curved, *WISE* TFR.

We use the *I*-band minus *WISE*-band color to correct the magnitudes and improve the scatter of the fits following Sorce et al. (2013). We use the residuals calculated in Equation (6) and then fit the correlation between the *I*-band and *WISE*-band color and the residuals as shown in Figure 12. Thus, we derive the correction to the magnitude that will produce an absolute magnitude from the TFR with the least scatter:

$$\Delta W1^{\rm color} = -0.470 - 0.561\left(I_T^{b,i,k} - W1_T^{b,i,k,a}\right), \quad (10a)$$

$$\Delta W2^{\rm color} = -0.874 - 0.617\left(I_T^{b,i,k} - W2_T^{b,i,k,a}\right). \quad (10b)$$

These are then used to adjust the input magnitudes as follows:

$$C_{W1,2} = W1, 2_T^{b,i,k,a} - \Delta W1, 2^{\rm color}. \quad (11)$$

We repeat the entire fitting process using C_{W1} and C_{W2} instead of $W1_T^{b,i,k,a}$ and $W2_T^{b,i,k,a}$. Using these pseudo-magnitudes reduces the ensemble scatter from 0.54 mag for W1 and 0.56 mag for W2 to an ensemble scatter of 0.46 mag for both bands, which compares well with the scatter of 0.44 mag after color term correction found in Sorce et al. (2013). The individual cluster zero points and scatters for the color-corrected pseudo-magnitudes are shown in the seventh and eighth columns of Tables 2 and 3. The value of 0.46 mag for the color-corrected ensemble scatter corresponds to a distance error of 23% in both

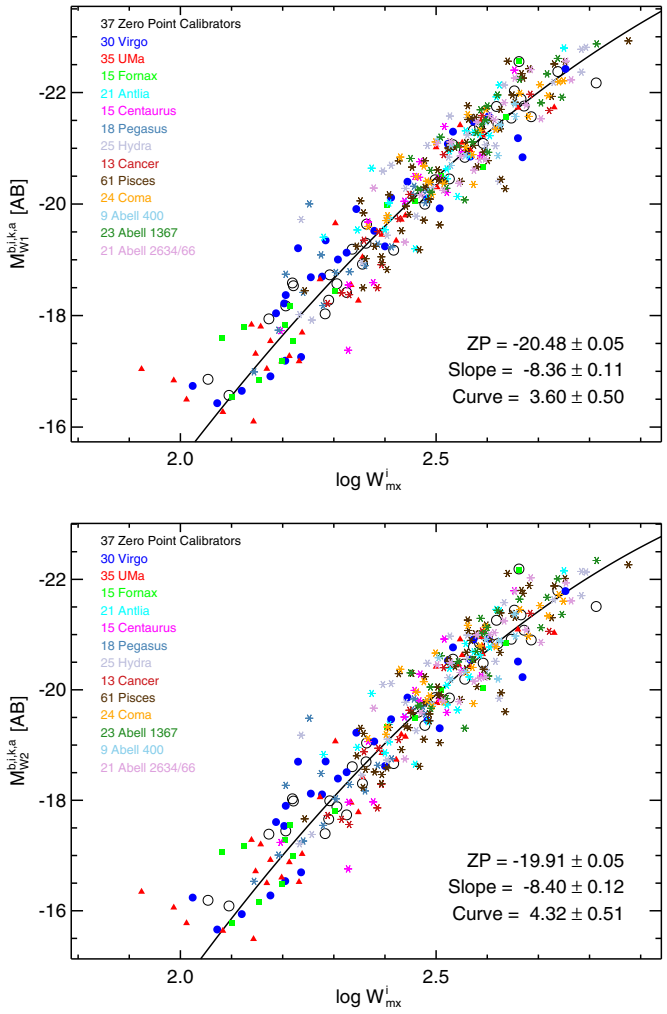

Figure 11. Curved TFR with the curve fit to the galaxies in 13 clusters and the absolute magnitude scale set by 37 zero-point calibrators for the W1 (top) and the W2 (bottom).

(A color version of this figure is available in the online journal.)

W1 and W2. In addition, the universal slopes for W1 and W2 are now nearly identical with a value of −9.12 for W1 and −9.11 for W2, whereas prior to color correction they were −9.56 for W1 and −9.74 for W2. The scatter in the zero-point sample was also reduced from 0.45 mag in W1 and 0.49 mag in W2 to 0.41 mag for W1 and 0.42 mag for W2. Compare these with a color-term-corrected scatter of 0.37 mag for the zero-point sample in Sorce et al. (2013). Figures 14 and 15 show the result of fitting

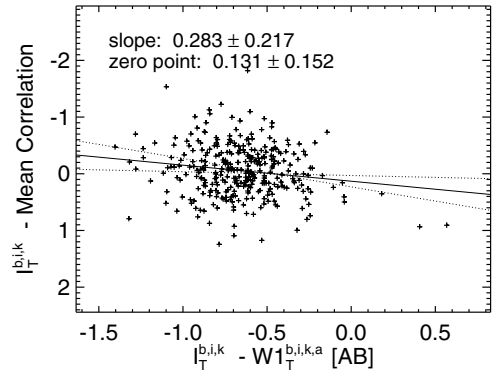

Figure 13. Deviations from the mean *I*-band TFR as a function of $I-\mathrm{W1}$ color (note that the slope is significant only at 1.2σ and the zero point is consistent with zero).

these pseudo-magnitudes. Since the color correction requires *I*-band photometry, the sample used for the color correction is reduced from 310 to 291 galaxies. The number of color-corrected galaxies in each cluster is listed in the sixth column of Tables 2 and 3.

This pseudo-magnitude calibration can now be expressed as

$$\mathcal{M}_{C_{W1}} = -(20.22 \pm 0.07) - (9.12 \pm 0.12)\big(\log W^i_{mx} - 2.5\big), \tag{12a}$$

$$\mathcal{M}_{C_{W2}} = -(19.63 \pm 0.07) - (9.11 \pm 0.12)\big(\log W^i_{mx} - 2.5\big). \tag{12b}$$

In order to derive the distance modulus for a given galaxy, we subtract Equation (12) from Equation (11):

$$\mu_{C_{W1,2}} = C_{W1,2} - \mathcal{M}_{C_{W1,2}}. \tag{13}$$

As a check for a color term in the *I*-band TFR, we plot the residuals with respect to the mean TFR, $\Delta M_I = M_I^{\mathrm{ens}} - \mathcal{M}_I^{b,i,k}$ (analogous to Equation (6)), as a function of the *I*-band minus W1 color in Figure 13. The formal error on the zero point is larger than the zero point itself. The slope has a value that is insignificant at 1.2σ. Thus, we conclude that an *I*-band color correction would have little or no effect.

We point out that this color correction has the effect of linearizing the *WISE* TFR and thereby removing the curvature we found in the pure *WISE* linear TFR. This color-corrected TFR has the advantage of lower scatter, while the curved TFR has the advantage that it does not rely on any other source of photometry. We refer to these color-corrected magnitudes as W1cc and W2cc in plots and tables to distinguish them from the pure *WISE* magnitudes W1 and W2.

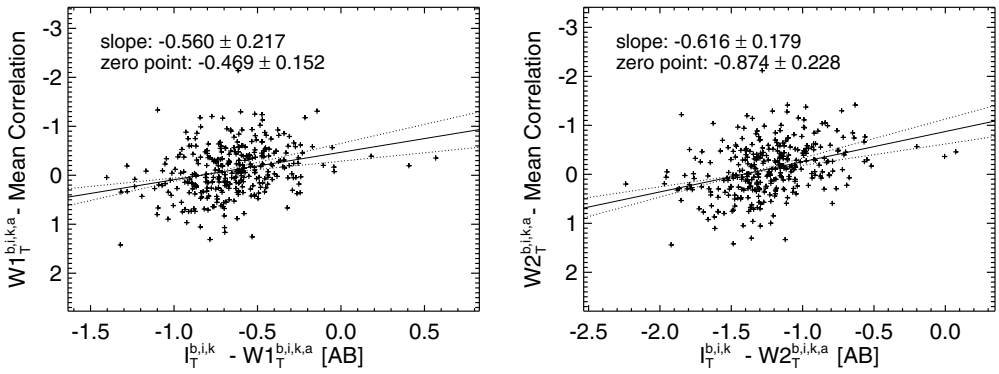

Figure 12. Deviations from the mean linear *WISE* TFRs as a function of $I-\mathrm{W1}$ (left) and $I-\mathrm{W2}$ (right) color.

Table 6
TFR Parameter Comparison

Reference	Photometry	Universal Slope/Curve				Zero Point		
		Ngal	Slope	Curve	rms	Ngal	Mag	rms
Tully & Courtois (2012)	I-band (Vega)	267	-8.81 ± 0.16	...	0.41	36	-21.39 ± 0.07	0.36
This work	I-band (Vega)	291	-8.95 ± 0.14	...	0.46	36	-21.34 ± 0.07	0.40
Sorce et al. (2013)	IRAC [3.6] (AB)	213	-9.74 ± 0.22	...	0.49	26	-20.34 ± 0.10	0.44
This work	W1 (AB)	310	-9.56 ± 0.12	...	0.54	37	-20.35 ± 0.07	0.45
This work	curved W1 (AB)	310	-8.36 ± 0.11	3.60 ± 0.50	0.52	37	-20.48 ± 0.05	0.39
Sorce et al. (2013)	$M_{C3.6\mu m}$ (AB)	213	-9.13 ± 0.22	...	0.44	26	-20.34 ± 0.08	0.37
This work	M_{CW1} (AB)	291	-9.12 ± 0.12	...	0.46	36	-20.22 ± 0.07	0.41
Lagattuta et al. (2013)	M_{corr} (AB)	568	-10.05	...	0.69	...	-19.54	...
This work	W2 (AB)	310	-9.74 ± 0.12	...	0.56	37	-19.76 ± 0.08	0.49
This work	M_{CW2} (AB)	291	-9.11 ± 0.12	...	0.46	36	-19.63 ± 0.07	0.42
This work	curved W2 (AB)	310	-8.40 ± 0.12	4.32 ± 0.51	0.55	37	-19.91 ± 0.05	0.43

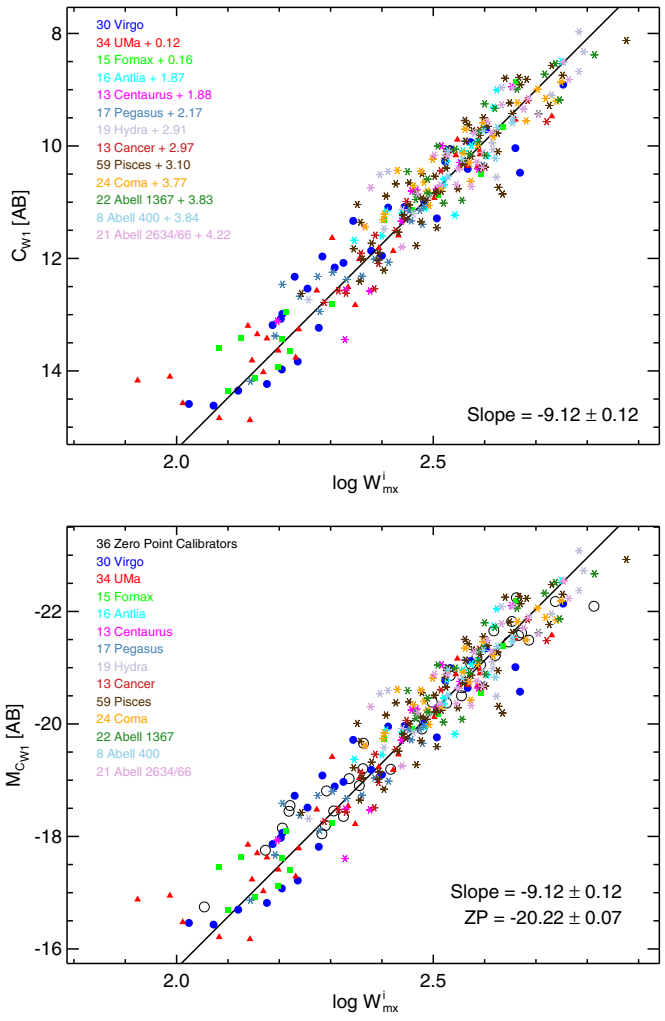

Figure 14. Linear TFR for W1 after adjustments for the color term with galaxies shifted to the apparent distance of Virgo (top) and on the absolute magnitude scale set by 37 zero-point calibrator galaxies (bottom).
(A color version of this figure is available in the online journal.)

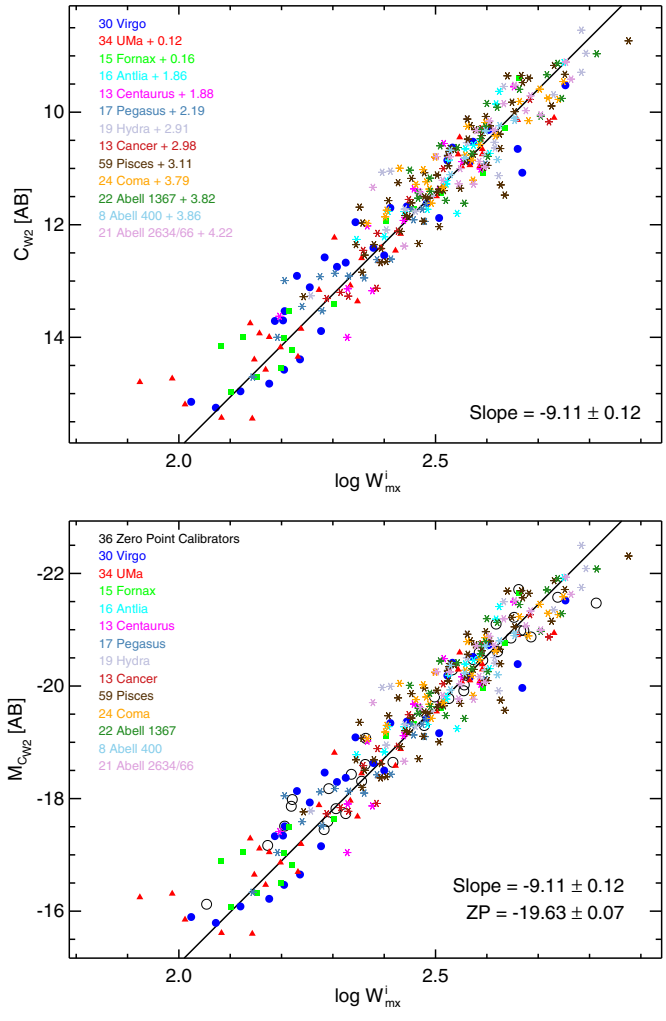

Figure 15. Linear TFR for W2 after adjustments for the color term with galaxies shifted to the apparent distance of Virgo (top) and on the absolute magnitude scale set by 37 zero-point calibrator galaxies (bottom).
(A color version of this figure is available in the online journal.)

7. COMPARISON WITH PREVIOUS CALIBRATIONS

We compare our results with previous TFR calibrations in Table 6. In the *I* band, the new calibration agrees with that from Tully & Courtois (2012) to well within the formal errors on the parameters. Our scatter is a little higher perhaps as a result of adding fainter galaxies. Comparing our W1 calibration to the IRAC [3.6] result in Sorce et al. (2013) shows consistency, both in the pure linear calibration parameters and in the color-corrected parameters. When we restrict our sample to the same

galaxies used in Sorce et al. (2013), we obtain the exact same scatter for the pure linear W1 TFR (0.49 mag). The only deviation of note is the color-corrected zero point, which is fainter for the W1. The zero-point samples are not identical, and it is possible that the color corrections couple with the *I* band in a different way owing to differences in filter responses between the IRAC [3.6] and W1 bandpasses.

The curved *WISE* TFR offers an improvement over the linear *WISE* TFR, although the rms scatter is still not as good as the color-corrected linear *WISE* TFR. We point out that the formal errors on the zero points for both the curved W1 and W2 TFRs are the lowest of all the fits and the scatter on the zero-point curved W1 calibration is marginally lower than for the color-corrected linear W1 TFR.

Lastly, we compare our results to the calibration in Lagattuta et al. (2013). This calibration was derived from *WISE* catalog photometry and not derived by the authors from their own photometry of the W1 images, as we have done here. The extended photometry is based on 2MASS apertures with a correction applied to account for the shallowness of 2MASS as compared to the *WISE* survey. No errors on the individual luminosity–line width correlation parameters are given, so we can only compare the scatter, which is greater by 50% than the calibration presented here. The zero point from that paper has been converted from Vega to AB magnitudes in Table 6.

8. THE HUBBLE CONSTANT, H_0

We can now use the TFR to derive distances and, with cosmological model-corrected recession velocities, estimate the local Hubble constant (H_0). Before we do this, we must consider any residual bias in our distance estimates due to our sample.

8.1. Distance Bias

The residual bias pointed out by Willick (1994) and discussed in detail in Sorce et al. (2013) is mitigated to some extent here since the current sample was selected using the 2MASS redshift survey complete to $K = 11.75$ (Huchra et al. 2012), effectively bringing the sample selection wavelength much closer to the *WISE* bands than the original sample, which was selected in the *B* band. However, we still must account for the fact that with a faint-end limit, more faint galaxies will be scattered into the sample than bright galaxies out of the sample.

The bias analysis carried out in Sorce et al. (2013) and Tully & Courtois (2012) is repeated here, but using a Schechter (1976) function with $\alpha = -1.0$ instead of -0.9. This value of α was arrived at by fitting the *WISE* W1 luminosity function of the combined nearest three calibration clusters: Virgo–Fornax–UMa (Tully & Courtois 2012, see their Section 3.1,). The bright-end characteristic magnitude for *WISE* is the same as was used for the IRAC [3.6] magnitudes: $M^{\star}_{W1} = -22$. Augmenting our sample selection with the 2MASS redshift survey allows us to assume a flat cutoff in the magnitudes as a function of line width. The driving factor in calculating the bias is the observed scatter in the TFR. Since the scatter in the color-corrected *WISE* TFR (for both W1 and W2) is the same as the *I*-band TFR (0.46 mag), we can use a simulation with this scatter to characterize the bias for all three TFRs. For the pure *WISE* linear and curved TFRs we use a scatter of 0.54 mag. A simulated TFR having the appropriate scatter is generated from these parameters and randomly sampled at a range of cutoff magnitude, $M^{\rm lim}$, which slides to brighter limits linearly as distance increases. The bias $\langle M\rangle_{\rm measured}$ is determined at intervals of $M^{\rm lim}$

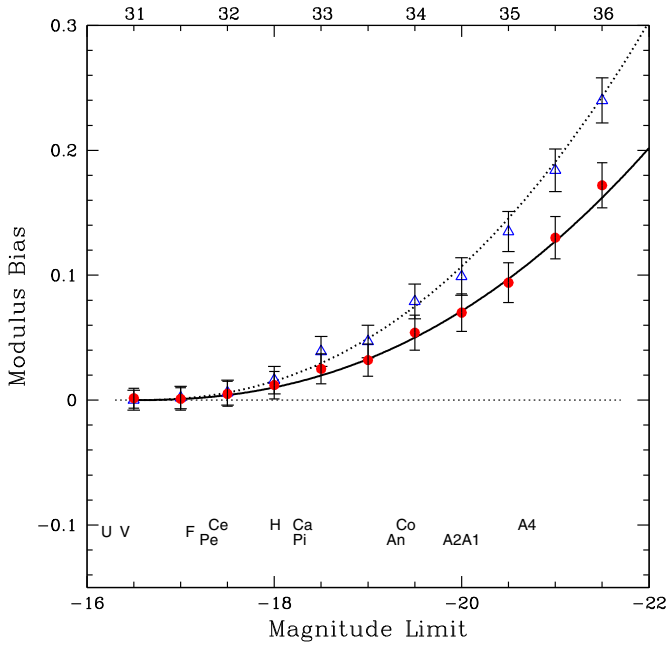

Figure 16. Bias $\langle M\rangle_{\rm measured}$ for the pure *WISE* TFR (blue open triangles) and color-corrected *WISE* TFR (solid red circles) as a function of absolute magnitude limit, which increases with distance. The solid curve is the empirical bias fit to the color-corrected *WISE* points, which has the form $b = 0.004(\mu - 31)^{2.3}$. The dotted curve is the empirical bias fit to the pure *WISE* data, which has the form $b = 0.006(\mu - 31)^{2.3}$. Letters at the bottom are codes for the 13 calibrating clusters (see second column of Table 5). Their horizontal positions indicate sample limits, and the vertical intercepts with the solid curve give the corresponding biases.

(A color version of this figure is available in the online journal.)

corresponding to increasing distance. At each cutoff limit, a random set of galaxies brighter than $M^{\rm lim}$ is drawn from the simulated TFR and used to calculate a new TFR. The average deviation from the input (true) TFR is the bias $\langle M\rangle_{\rm measured}$. This bias is plotted in Figure 16 for both the pure (open blue triangles) and color-corrected (solid red circles) *WISE* TFR. The solid and dotted curves are normalized to zero at a distance modulus of $\mu = 31$ (Virgo), where we are assumed to be complete. These curves are described by the formulae

$$b_{\rm pure} = 0.006(\mu - 31)^{2.3} \tag{14a}$$

$$b_{\rm cc} = 0.004(\mu - 31)^{2.3} \tag{14b}$$

where μ is the distance modulus to the object (galaxy or cluster) derived using one of Equation (5), (8), or (13). This bias function is slightly steeper than that seen in Sorce et al. (2013), having an exponent of 2.3 instead of 2 as a result of an increase in the assumed scatter from 0.40 to 0.46 mag. The letter codes in Figure 16 show the cutoff magnitudes for the calibration clusters (see the second column of Table 5) by their horizontal placement and the resulting bias by the vertical intersection with the solid line. For a galaxy in the field, the corrected distance modulus is thus

$$\mu^{c}_{\rm pure} = \left(W1, 2^{b,i,k,a}_{T} - \mathcal{M}^{b,i,k,a}_{W1,2}\right) + 0.006\Big[\left(W1, 2^{b,i,k,a}_{T} - \mathcal{M}^{b,i,k,a}_{W1,2}\right) - 31\Big]^{2.3}, \tag{15a}$$

$$\mu^{c}_{cc} = (C_{W1,2} - \mathcal{M}_{C_{W1,2}}) + 0.004[(C_{W1,2} - \mathcal{M}_{C_{W1,2}}) - 31]^{2.3}. \tag{15b}$$

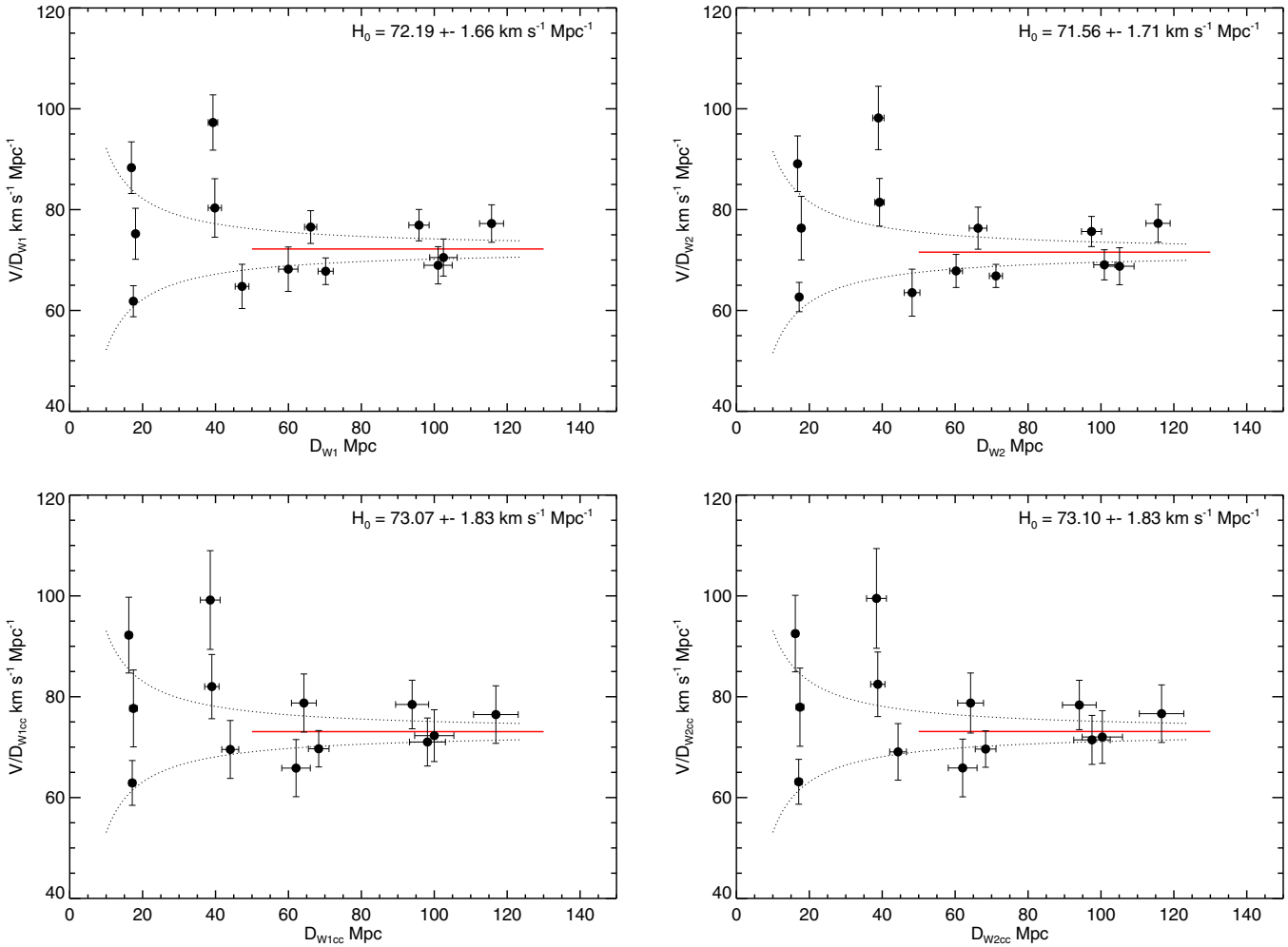

Figure 17. Hubble parameter as a function of distance for the *WISE* W1 curved TFR (top left), W2 curved TFR (top right), W1 color-corrected TFR (W1cc, bottom left), and W2 color-corrected TFR (W2cc, bottom right).

(A color version of this figure is available in the online journal.)

We list the biases for the pure *WISE* and the color-corrected *WISE* magnitudes in the third column of Table 7. Now we turn to using our calibrating clusters to estimate H_0.

8.2. H_0 From Clusters

As we have already pointed out, we expect a systematic problem with using the linear, uncorrected *WISE* TFR (see Sections 4 and 5) to calculate H_0. We present these values to illustrate this systematic, but we concentrate on the curved *WISE* TFR or the color-corrected *WISE* TFR for calculating distances used to derive H_0. With distance moduli and hence distances for each cluster derived from the ensemble of galaxies used to calibrate the cluster (see Table 7), we can use the ensemble velocity to calculate a Hubble constant, H_0, for each cluster. We use the bi-weight method described in Beers et al. (1990) to derive a robust ensemble velocity for each cluster. These velocities are then shifted to the cosmic microwave background (CMB) frame and adjusted based on a cosmological model that assumes $\Omega_m = 0.27$ and $\Omega_\Lambda = 0.73$. The cosmological adjustments are admittedly small, but not insignificant. These velocities and associated errors are listed in Table 7 in the second column, labeled $V_{\rm mod}$ (see Tully et al. 2013, Equation (14)) to indicate the adjustment for the cosmological model specified previously. We calculate $H_0 = V_{\rm mod}/D_{\rm Mpc}$ for each cluster as shown in the seventh column of the aforementioned table and plotted for *WISE* and the *I* band in Figures 17 and 18.

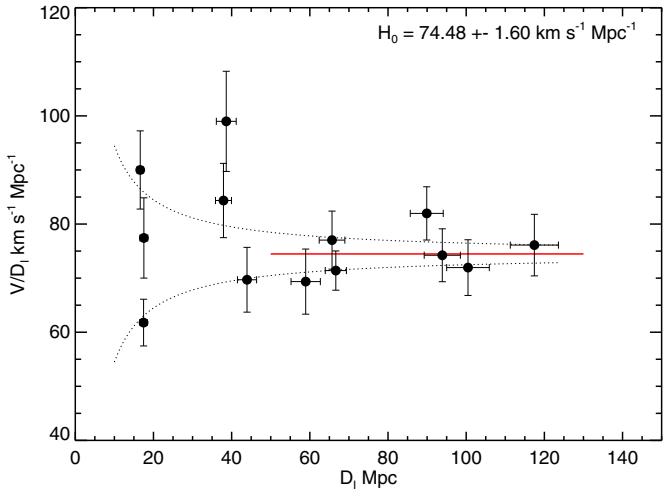

Figure 18. Hubble parameter as a function of distance for the *I* band.

(A color version of this figure is available in the online journal.)

Examining Figures 17 and 18, we see that the nearer clusters have a large scatter while those beyond 50 Mpc

Table 7
Cluster Distances and H_0 Data

Cluster[a]	V_{mod}[b]	Bias[c]	DM[d]	D_{Mpc}[e]	V_{mod}/D_{Mpc}[f]	TFR Band[g]
Virgo	1495. ± 37.	0.000	31.14 ± 0.08	16.93 ± 0.59	88.32 ± 5.47	W1cur
		0.000	31.12 ± 0.08	16.78 ± 0.59	89.09 ± 5.52	W2cur
		0.000	31.05 ± 0.12	16.21 ± 0.85	92.22 ± 7.51	W1cc
		0.000	31.04 ± 0.12	16.16 ± 0.86	92.52 ± 7.59	W2cc
		0.000	31.10 ± 0.11	16.61 ± 0.85	90.00 ± 7.23	*I*-band
U Ma	1079. ± 14.	0.000	31.21 ± 0.07	17.45 ± 0.56	61.83 ± 2.88	W1cur
		0.000	31.18 ± 0.07	17.22 ± 0.55	62.66 ± 2.91	W2cur
		0.000	31.17 ± 0.12	17.16 ± 0.92	62.90 ± 4.44	W1cc
		0.000	31.16 ± 0.12	17.09 ± 0.92	63.13 ± 4.45	W2cc
		0.000	31.21 ± 0.12	17.47 ± 0.93	61.78 ± 4.32	*I*-band
Fornax	1358. ± 45.	0.000	31.28 ± 0.10	18.06 ± 0.83	75.21 ± 6.21	W1cur
		0.000	31.25 ± 0.10	17.79 ± 0.81	76.33 ± 6.31	W2cur
		0.000	31.21 ± 0.13	17.48 ± 1.04	77.68 ± 7.63	W1cc
		0.000	31.21 ± 0.13	17.43 ± 1.05	77.93 ± 7.75	W2cc
		0.000	31.22 ± 0.13	17.54 ± 1.00	77.43 ± 7.42	*I*-band
Antlia	3198. ± 74.	0.060	33.00 ± 0.07	39.81 ± 1.31	80.33 ± 4.67	W1cur
		0.060	32.97 ± 0.07	39.26 ± 1.30	81.45 ± 4.73	W2cur
		0.040	32.96 ± 0.11	38.99 ± 1.97	82.01 ± 6.37	W1cc
		0.040	32.94 ± 0.11	38.78 ± 1.96	82.47 ± 6.40	W2cc
		0.040	32.89 ± 0.12	37.91 ± 2.04	84.35 ± 6.87	*I*-band
Centaurus	3823. ± 82.	0.000	32.97 ± 0.09	39.30 ± 1.56	97.28 ± 6.19	W1cur
		0.000	32.95 ± 0.09	38.94 ± 1.56	98.18 ± 6.29	W2cur
		0.000	32.93 ± 0.16	38.55 ± 2.71	99.18 ± 9.79	W1cc
		0.000	32.92 ± 0.16	38.42 ± 2.72	99.50 ± 9.89	W2cc
		0.000	32.93 ± 0.15	38.62 ± 2.54	98.99 ± 9.26	*I*-band
Pegasus	3062. ± 78.	0.000	33.37 ± 0.10	47.27 ± 2.09	64.77 ± 4.72	W1cur
		0.000	33.42 ± 0.10	48.19 ± 2.15	63.53 ± 4.66	W2cur
		0.000	33.22 ± 0.12	44.04 ± 2.32	69.54 ± 5.74	W1cc
		0.000	33.23 ± 0.12	44.34 ± 2.29	69.06 ± 5.61	W2cc
		0.000	33.21 ± 0.12	43.93 ± 2.45	69.70 ± 5.99	*I*-band
Hydra	4088. ± 72.	0.015	33.89 ± 0.07	59.95 ± 1.77	68.19 ± 3.32	W1cur
		0.015	33.90 ± 0.06	60.26 ± 1.76	67.84 ± 3.28	W2cur
		0.010	33.97 ± 0.14	62.09 ± 3.91	65.84 ± 5.67	W1cc
		0.010	33.96 ± 0.14	62.06 ± 3.95	65.87 ± 5.72	W2cc
		0.010	33.85 ± 0.14	58.94 ± 3.75	69.36 ± 6.02	*I*-band
Pisces	4759. ± 39.	0.030	34.23 ± 0.06	70.21 ± 1.77	67.78 ± 2.32	W1cur
		0.030	34.26 ± 0.06	71.19 ± 1.80	66.85 ± 2.29	W2cur
		0.020	34.17 ± 0.09	68.30 ± 2.83	69.68 ± 3.61	W1cc
		0.020	34.17 ± 0.09	68.36 ± 2.84	69.62 ± 3.61	W2cc
		0.020	34.12 ± 0.09	66.65 ± 2.70	71.40 ± 3.63	*I*-band
Cancer	5059. ± 82.	0.030	34.10 ± 0.08	66.10 ± 2.43	76.54 ± 4.21	W1cur
		0.030	34.11 ± 0.08	66.28 ± 2.42	76.32 ± 4.17	W2cur
		0.020	34.04 ± 0.12	64.24 ± 3.41	78.75 ± 5.76	W1cc
		0.020	34.04 ± 0.12	64.24 ± 3.54	78.75 ± 5.95	W2cc
		0.020	34.09 ± 0.11	65.68 ± 3.28	77.03 ± 5.37	*I*-band
A400	7228. ± 97.	0.165	35.05 ± 0.08	102.52 ± 3.92	70.50 ± 3.79	W1cur
		0.165	35.11 ± 0.08	105.10 ± 3.98	68.77 ± 3.67	W2cur
		0.110	35.00 ± 0.12	100.00 ± 5.38	72.28 ± 5.14	W1cc
		0.110	35.01 ± 0.12	100.37 ± 5.53	72.01 ± 5.22	W2cc
		0.110	35.01 ± 0.12	100.46 ± 5.45	71.95 ± 5.15	*I*-band
A1367	6969. ± 93.	0.120	35.02 ± 0.06	101.06 ± 2.93	68.96 ± 3.01	W1cur
		0.120	35.02 ± 0.06	100.93 ± 2.90	69.05 ± 2.99	W2cur
		0.080	34.96 ± 0.11	98.13 ± 4.93	71.02 ± 4.76	W1cc
		0.080	34.95 ± 0.11	97.54 ± 5.00	71.44 ± 4.86	W2cc
		0.080	34.86 ± 0.11	93.89 ± 4.63	74.23 ± 4.89	*I*-band
Coma	7370. ± 76.	0.060	34.91 ± 0.06	95.81 ± 2.72	76.92 ± 3.07	W1cur
		0.060	34.94 ± 0.06	97.41 ± 2.74	75.66 ± 2.99	W2cur
		0.040	34.86 ± 0.11	93.93 ± 4.53	78.46 ± 4.82	W1cc
		0.040	34.87 ± 0.11	94.06 ± 4.62	78.36 ± 4.90	W2cc
		0.040	34.77 ± 0.10	89.91 ± 4.22	81.97 ± 4.92	*I*-band
A2634/66	8938. ± 164.	0.105	35.32 ± 0.06	115.72 ± 3.36	77.24 ± 3.77	W1cur
		0.105	35.32 ± 0.06	115.66 ± 3.32	77.28 ± 3.74	W2cur

Table 7
(Continued)

Cluster[a]	V_{mod}[b]	Bias[c]	DM[d]	D_{Mpc}[e]	V_{mod}/D_{Mpc}[f]	TFR Band[g]
		0.070	35.34 ± 0.12	116.90 ± 6.12	76.46 ± 5.71	W1cc
		0.070	35.33 ± 0.12	116.63 ± 6.10	76.64 ± 5.71	W2cc
		0.070	35.35 ± 0.12	117.44 ± 6.16	76.11 ± 5.69	*I*-band

Notes.
[a] Cluster name.
[b] Mean cluster cosmology-corrected velocity in CMB frame (km s^{-1}).
[c] Bias, *b* (mag).
[d] Bias-corrected distance modulus (mag).
[e] Cluster distance (Mpc).
[f] Hubble parameter (km s^{-1} Mpc^{-1}).
[g] Source photometry.

($V_{mod} > 4000$ km s^{-1}) have a smaller scatter. This is simply the result of the peculiar motions induced by local structures in our supercluster complex (the transformation of velocities to the cosmic microwave background frame gives all nearby galaxies large peculiar velocities). We plot an error envelope of 200 km s^{-1} as a dotted line in each figure to show the effect of peculiar velocities on H_0 as a function of distance. In order to derive an estimate of the universal Hubble constant, we consider only clusters beyond 50 Mpc and average the log of their resulting H_0 values since the errors are predominantly in the distance and symmetric about the distance modulus. We find an error-weighted, logarithmic-averaged Hubble constant of $H_0 = 73.1 \pm 1.8$ km s^{-1} Mpc^{-1} for both W1cc and W2cc. For the curved pure *WISE* TFR, we get $H_0 = 72.2 \pm 1.7$ km s^{-1} Mpc^{-1} for W1 and $H_0 = 71.6 \pm 1.7$ km s^{-1} Mpc^{-1} for W2. For the *I* band we get a larger value of $H_0 = 74.5 \pm 1.6$ km s^{-1} Mpc^{-1}. This amounts to a range of $\sim \pm 1.5\%$ from a logarithmic average of 72.9 km s^{-1} Mpc^{-1} derived from all five of these cluster TFR H_0 values.

Using the linear, pure *WISE* TFR, we derive values of $H_0 = 70.6 \pm 1.6$ km s^{-1} Mpc^{-1} for W1 and $H_0 = 69.8 \pm 1.6$ km s^{-1} Mpc^{-1} for W2. These values are low compared with either the curved or the color-corrected TFR values, as expected from a systematic that biases distant clusters toward larger distances.

All the error bars listed above are formal statistical error bars and do not account for systematics. The calibration clusters may still be strongly influenced by local large-scale structures and thus may not provide the most robust estimate of H_0. In addition, there are only seven clusters beyond 50 Mpc, and small number statistics may play a role. Systematic errors are discussed in detail in the next subsection when we extend our reach well beyond local structures and use a larger sample of supernova host galaxies to estimate H_0.

8.3. H_0 From Supernovae

The precision of distances derived from SNe Ia offers a better avenue for determining H_0 free from the small number statistics that influence the determination of H_0 from seven nearby galaxy clusters. In order to exploit the reach of SNe Ia, which is well beyond the local velocity perturbations we see in our cluster H_0 estimations, we must tie the SN Ia distance scale to the distance scale established by the TFR. Even though there are few SNe Ia that have been detected in nearby galaxies, there are 56 SNe Ia that have been detected in host galaxies within the Cosmic Flows sample (see Section 2.2). These galaxies also have *I*-band photometry allowing the color-corrected MIR TFR to be used in addition to the curved pure *WISE* TFR. This permits an accurate determination of the offset between the SN Ia and TFR distance moduli.

We use the UNION2 sample of SNe Ia (Amanullah et al. 2010) for this comparison. This sample encompasses distances out to beyond $z \sim 1$ and includes all the SNe Ia hosts from the Cosmic Flows galaxy sample. We can improve our statistical error in the situation where there are multiple SNe Ia within a cluster. Of the 13 clusters used to calibrate the TFR, 8 have had one or more SNe Ia erupt within one or more member galaxies (see Table 2 of Sorce et al. 2012b). We use the same bi-weight method from Beers et al. (1990) to derive robust averages for the group velocities and distance moduli based on the SNe Ia and based on the TFR. We also use SN Ia hosts not in clusters. These individual hosts will have lower weight by virtue of their higher statistical error; however, the ensemble will help to constrain the offset.

Figure 19 presents the comparison of the TFR distance moduli derived from the *WISE* passbands and the SN Ia distance moduli for the eight clusters and 56 individual galaxies, while Figure 20 shows the same comparison for the *I* band. The distance modulus offsets are derived from error-weighted fits with the slope fixed at a value of 1. The clusters have the largest influence on these offsets owing to their low statistical errors, yet the resultant fits appear to bisect the distributions for the individual galaxies as well. The resulting distance modulus offsets are identical for the curved TFR for W1 and W2: 0.57 ± 0.02 mag. The rms values are calculated only from the individual galaxy residuals and are 0.45 mag for W1 and 0.48 mag for W2. For the color-corrected TFR, we find an offset of 0.53 ± 0.03 mag for W1cc and 0.52 ± 0.03 mag for W2cc and rms values of 0.53 mag for W1cc and 0.54 mag for W2cc. For the *I* band the offset is 0.51 ± 0.03 mag with a scatter of 0.55 mag, which is very close to the values shown in the top panel of Figure 2 from Courtois & Tully (2012), which is also derived only from the SN Ia–TFR offset.

As was pointed out by Courtois & Tully (2012), the scatters in the linear TFR offset data are ~10% larger than expected from the combination of the individual scatters in the linear TFRs (0.46 mag for the color-corrected W1, 2 and the *I* band) and the SN Ia (0.20 mag) distance scales. We do not present the offset data for the pure *WISE* linear TFR, but these scatters are even larger at 0.56 mag for W1 and 0.58 mag for W2. For the curved pure *WISE* TFRs, the SN Ia–TFR distance modulus scatter is actually less than expected when adding the TFR scatter (0.52 mag for curved W1 and 0.55 mag for curved W2) in quadrature with the SN Ia distance modulus scatter. In fact,

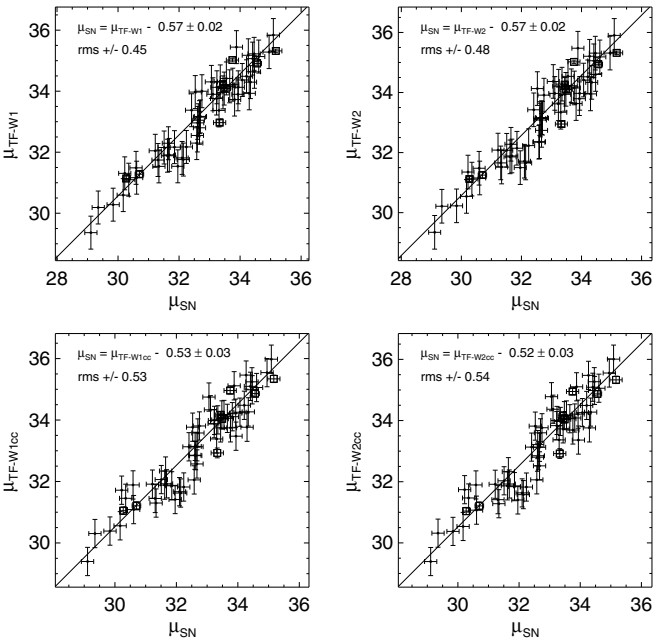

Figure 19. Distance modulus offsets derived from the SN Ia sample and from the TFR for the *WISE* W1 curved TFR (top left), W2 curved TFR (top right), W1 color-corrected TFR (bottom left), and W2 color-corrected TFR (bottom right). Open squares indicate the ensemble robust averages for the eight clusters that have had one or more SNe Ia erupt within member galaxies. Solid circles indicate individual hosts within which an SN Ia from the UNION2 sample has erupted. Note the small scatters and low formal errors using the curved pure *WISE* TFRs.

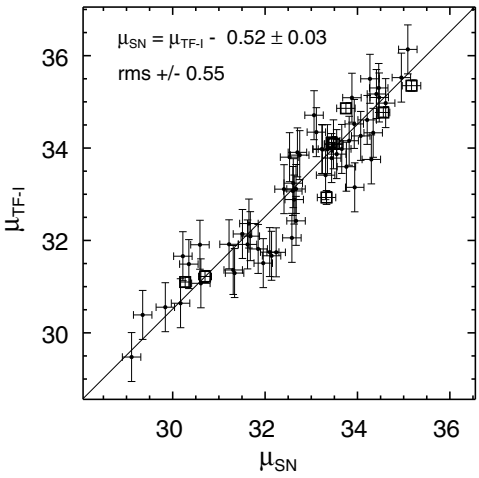

Figure 20. Distance modulus offset derived from the SN Ia sample and from the TFR for the *I* band. Symbols have the same meaning as in Figure 19.

the scatter in the curved W1 is 20% less than the scatter in the *I* band. The scatter in all of these offsets has been calculated with the exact same sample and using the exact same method. With a sample of 56 galaxies, it is hard to explain this away with small number statistics. It is possible that this results from a better alignment between the clusters and the individual galaxies using the curved TFRs, although this is not obvious from Figure 19. As a test of the TFR, this lower scatter is strong evidence in favor of using the curved pure *WISE* TFR for deriving distances.

The formal errors on the curved TFR W1 and W2 distance modulus offsets correspond to an error in H_0 of $0.7\,\mathrm{km\,s^{-1}\,Mpc^{-1}}$, while the formal errors on the color-corrected and *I*-band offsets correspond to an error in H_0 of

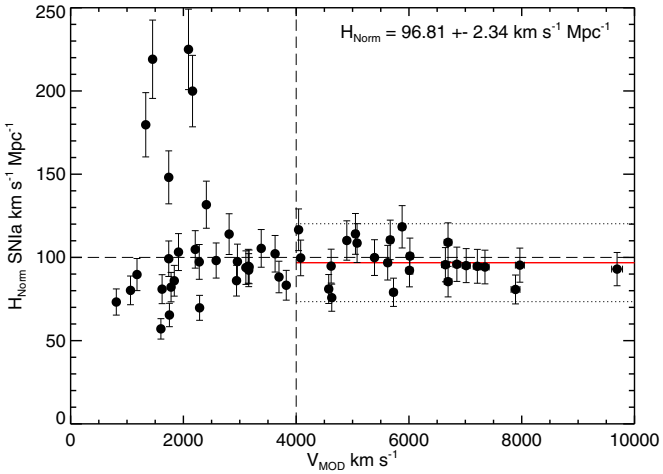

Figure 21. Hubble parameter normalization as a function of recession velocity using only the UNION2 SN Ia distance moduli (Amanullah et al. 2010) for galaxies in common with the Cosmic Flows sample. Here we are only verifying the normalization of this sample at 100 km s^{-1} Mpc^{-1} for our subsample of SN Ia host galaxies. This plot shows that, for our subsample, the normalization is less than the nominal value, and thus we need to apply an offset of -3.2 ± 2.3 km s^{-1} Mpc^{-1} when we renormalize the SN Ia hosts with the TFR distances.

(A color version of this figure is available in the online journal.)

$1.1\,\mathrm{km\,s^{-1}\,Mpc^{-1}}$. Using the curved TFR W1 and W2 distance modulus offsets represents a 30% reduction in the H_0 error budget.

Figure 21 shows the calculation of the normalization of the Hubble constant, H_{Norm}, using only the SNe Ia from the UNION2 sample that overlap with the Cosmic Flows sample. The overlap zero point is not, in fact, $H_{\mathrm{Norm}} = 100\,\mathrm{km\,s^{-1}\,Mpc^{-1}}$, but slightly less: $H_{\mathrm{Norm}} = 96.8 \pm 2.3\,\mathrm{km\,s^{-1}\,Mpc^{-1}}$, an offset of $3.2\,\mathrm{km\,s^{-1}\,Mpc^{-1}}$. A similar offset was found by Courtois & Tully (2012) when setting the distance zero point using the *I*-band TFR. Once we apply this normalization offset, we derive values of $H_0 = 73.7 \pm 2.4\,\mathrm{km\,s^{-1}\,Mpc^{-1}}$ for W1 and W2, $H_0 = 75.2 \pm 2.5\,\mathrm{km\,s^{-1}\,Mpc^{-1}}$ for W1cc and $H_0 = 75.5 \pm 2.5\,\mathrm{km\,s^{-1}\,Mpc^{-1}}$ for W2cc, and $H_0 = 75.9 \pm 2.5\,\mathrm{km\,s^{-1}\,Mpc^{-1}}$ for the *I* band. These errors are the combination in quadrature of the SN Ia–TFR offset H_0 error (stated in the previous paragraph) and the UNION2 normalization offset uncertainty shown in Figure 21. Since the two curved pure *WISE* values and the *I*-band value are independent from one another, we are allowed to perform a log average of these three values. This gives our best estimate of the Hubble constant of $H_0 = 74.4 \pm 1.4$ km s^{-1} Mpc^{-1}. Here the error is the statistical error in the mean value.

For completeness we present the values derived with the linear pure *WISE* TFR. Using the same SN Ia hosts, we derive $H_0 = 73.0 \pm 2.7$ km s^{-1} Mpc^{-1} for W1 and $H_0 = 72.7 \pm 2.7$ km s^{-1} Mpc^{-1} for W2. These values are low as expected from the systematic bias caused by using a linear fit on a curved TFR.

Systematic errors need to be accounted for in the H_0 calculations. By using IR photometry, we reduce the uncertainties due to dust significantly. Since we have used three bandpasses for these calculations, we can use the differences to estimate the systematic errors between bands. Based on the range of H_0 we derive for all three bandpasses, we estimate the inter-band systematic to be ± 1.1 km s^{-1} Mpc^{-1}. The other source of systematic error is the error on the distance to the LMC,

Table 8
Hubble Constant Comparison

Reference	TFR Band[a]	Clusters[b,c]	SNe Ia[c,d]
Tully & Courtois (2012)	*I*-band	75.1 ± 1.0	...
Courtois & Tully (2012)	*I*-band	...	75.9 ± 3.8
This work	*I*-band	74.5 ± 1.6	75.9 ± 2.5
Sorce et al. (2013)	[3.6]cc	74 ± 4	...
Sorce et al. (2012b)	[3.6]cc	...	75.2 ± 3.0
This work	W1lin	71 ± 2	73.0 ± 2.7
This work	W2lin	70 ± 2	72.7 ± 2.7
This work	W1cc	73 ± 2	75.1 ± 2.5
This work	W2cc	73 ± 2	75.1 ± 2.5
This work	W1cur	72 ± 2	73.7 ± 2.4
This work	W2cur	72 ± 2	73.7 ± 2.4
This work	⟨W1cur,W2cur,I⟩	73 ± 1	74.4 ± 2.8[e]

Notes.
[a] Here "lin" indicates linear TFR, "cc" indicates optical–MIR color-corrected photometry, "cur" indicates curved TFR.
[b] Seven clusters with $V_{\rm mod} > 4000$ km s^{-1}.
[c] Units of km s^{-1} Mpc^{-1}.
[d] Offsets applied to UNION2 SN Ia sample (Amanullah et al. 2010).
[e] Includes statistical and systematic errors.

which forms the basis for our TFR distance scale and has a systematic of ± 0.033 mag (Freedman et al. 2012), which also corresponds to an error on H_0 of ± 1.1 km s^{-1} Mpc^{-1}. Another error is the formal TFR zero-point error (see Table 6, eighth column), which is 0.05 mag, which corresponds to an error on H_0 of ± 1.8 km s^{-1} Mpc^{-1}. Adding these in quadrature gives a systematic error on H_0 of ± 2.4 km s^{-1} Mpc^{-1}. Thus, our best value is $H_0 = 74.4 \pm 1.4$(stat) $\pm$ 2.4(sys) km s^{-1} Mpc^{-1}. We can add the statistical and systematic errors in quadrature to give a total error of ± 2.8 km s^{-1} Mpc^{-1}, which amounts to a percentage error of $\sim$4%.

8.4. Comparison with Previous H_0 Results

Our cluster H_0 values compare well with previous determinations for clusters calibrated with the TFR as shown in the third column of Table 8. Here we are listing statistical errors only. For the *I* band, Tully & Courtois (2012) find $H_0 = 75.1 \pm 1.0$ km s^{-1} Mpc^{-1}, which agrees to within 1% of our value of 74.5 ± 1.6 km s^{-1} Mpc^{-1}. Sorce et al. (2013) used the color-corrected IRAC [3.6] band ([3.6]cc) to derive $H_0 = 73.8 \pm 1.1$ km s^{-1} Mpc^{-1}, which is well within the statistical error bars (and also within 1%) of our color-corrected W1 (W1cc) value of 73.1 ± 1.8 km s^{-1} Mpc^{-1}. Our pure *WISE* curved TFR cluster H_0 values are low although still in statistical agreement with the other values.

Comparing the H_0 values derived by bringing the UNION2 sample onto the TFR distance scale also shows good consistency, as can be seen in the fourth column of Table 8. The *I*-band value from Courtois & Tully (2012) of $H_0 = 75.9 \pm 3.8$ km s^{-1} Mpc^{-1} is identical to our value, although their error bar includes systematic errors and so appears larger than ours. The color-corrected IRAC [3.6] value presented in Sorce et al. (2012b) of $H_0 = 75.2 \pm 3.0$ km s^{-1} Mpc^{-1} is less than two-tenths of a percent different from our value of 75.1 ± 2.5 km s^{-1} Mpc^{-1} derived from color-corrected W1.

What is new is using the uncorrected curved TFR to derive values of H_0. While these values are low for the seven clusters used to calibrate the TFR, when used to renormalize the UNION2 SN Ia sample, the values agree well with current best estimates of H_0 (see below). The other advantage of using the uncorrected curved TFR for *WISE* is that it is truly independent of the *I* band, unlike the color-corrected TFR values, and thus we can average all three bands (in the logarithm) to derive a more robust value of H_0. This is presented in the last column of the last row of Table 8, and the error includes both statistical and systematic errors.

It is interesting to note that Sakai et al. (2000) give a value of $H_0 = 71 \pm 4$ (random) ± 7 (systematic) km s^{-1} Mpc^{-1} using a weighted average of their four-band ($BVIH_{-0.5}$) TFRs fit with linear relations. At the end of their Section 5.2.1, they give a value of $H_0 = 73 \pm 2$ (random) km s^{-1} Mpc^{-1} for a curved *I*-band TFR. This is higher than the H_0 derived from linear TFRs and closer to current estimates, including our own.

A current independent estimate for H_0 that is useful for comparison is that presented in Freedman et al. (2012): $H_0 = 74.3 \pm 1.5$(stat) $\pm$ 2.1(sys) km s^{-1} Mpc^{-1}, which has a percentage systematic error of 2.8%. All of the SN Ia-derived H_0 values we present here agree with this value to within the errors. Another value to compare with is that derived from the *Planck* mission and presented in Collaboration et al. (2013): $H_0 = 67.3 \pm 1.2$ km s^{-1} Mpc^{-1}. Our lowest value of H_0 is the one derived from seven clusters in the uncorrected curved W2 band (71.6 ± 1.7 km s^{-1} Mpc^{-1}). This value is 3.6σ high using their error bar and 2.5σ high using our error bar. Our best result of $H_0 = 74.4 \pm 2.8$(stat and sys) km s^{-1} Mpc^{-1} is 5.9σ high using their error bar and 2.5σ high using our error estimate. Our data do not favor such a low value of H_0. We can also compare with another CMD H_0 value from Hinshaw et al. (2013), who quote $H_0 = 69.32 \pm 0.80$ (stat) km s^{-1} Mpc^{-1} in their Table 4. This value is closer to our value, but a tension still exists. Relativistic corrections for foreground lensing in the CMB analyses may resolve this tension (Clarkson et al. 2014).

9. CONCLUSIONS

We have derived a calibration of the absolute magnitude–line width relation for the *WISE* W1 and W2 filters. The raw, linear calibration, using only *WISE* photometry that is aperture corrected, is *k*-corrected, and has been corrected for internal and external extinction, gives

$$M_{W1}^{b,i,k,a} = -(20.35 \pm 0.07) - (9.56 \pm 0.12)\big(\log W_{mx}^{i} - 2.5\big), \quad (16a)$$

$$M_{W2}^{b,i,k,a} = -(19.76 \pm 0.08) - (9.74 \pm 0.12)\big(\log W_{mx}^{i} - 2.5\big). \quad (16b)$$

These calibrations show a scatter of 0.54 magnitudes in W1 and 0.56 magnitudes in W2.

The *I*-band sample grew by 24 galaxies (9%) compared to the previous calibration, and so we updated it to

$$M_{I}^{b,i,k,e} = -(21.34 \pm 0.07) - (8.95 \pm 0.14)\big(\log W_{mx}^{i} - 2.5\big). \quad (17)$$

This calibration has a scatter of 0.46 mag.

We find evidence for curvature in the MIR TFR based on a comparison between calibration cluster distances generated using linear TFRs in the *I* band and in the *WISE* W1 and W2 bands. We use the ensemble of cluster galaxies shifted to have an apparent distance of Virgo to fit this curved TFR and find the

following curved TFRs for W1 and W2:

$$\mathcal{M}_{W1}^{b,i,k,a} = -(20.48 \pm 0.05) - (8.36 \pm 0.11)\big(\log W_{mx}^{i} - 2.5\big) + (3.60 \pm 0.50)\big(\log W_{mx}^{i} - 2.5\big)^2, \quad (18a)$$

$$\mathcal{M}_{W2}^{b,i,k,a} = -(19.91 \pm 0.05) - (8.40 \pm 0.12)\big(\log W_{mx}^{i} - 2.5\big) + (4.32 \pm 0.51)\big(\log W_{mx}^{i} - 2.5\big)^2. \quad (18b)$$

These calibrations have a scatter of 0.52 mag for W1 and 0.55 mag for W2, an improvement over the pure linear TFRs. The formal errors on the zero-point calibration are the smallest of all the calibrations derived here.

Following previous work on calibrating the TFR in the MIR (Sorce et al. 2013), we apply an optical–MIR color correction to our raw W1 and W2 magnitudes in order to reduce the scatter. The corrections have the form

$$\Delta W1^{\rm color} = -0.470 - 0.561\big(I_T^{b,i,k} - W1_T^{b,i,k,a}\big), \quad (19a)$$

$$\Delta W2^{\rm color} = -0.874 - 0.617\big(I_T^{b,i,k} - W2_T^{b,i,k,a}\big), \quad (19b)$$

where $I_T^{b,i,k}$ values are derived from *I*-band imaging. These are then used to adjust the input magnitudes as follows:

$$C_{W1,2} = W1, 2_T^{b,i,k,a} - \Delta W1, 2^{\rm color}. \quad (20)$$

We used these pseudo-magnitudes to generate color-corrected linear calibrations of the form

$$M_{C_{W1}} = -(20.22 \pm 0.07) - (9.12 \pm 0.12)\big(\log W_{mx}^{i} - 2.5\big), \quad (21a)$$

$$M_{C_{W2}} = -(19.63 \pm 0.07) - (9.11 \pm 0.12)\big(\log W_{mx}^{i} - 2.5\big). \quad (21b)$$

These both show a scatter of 0.46 mag, similar to the *I*-band scatter. These equations represent the most accurate calibration of the luminosity–line width relation available for *WISE* data at this time.

We investigate a residual bias in the TFRs resulting from a flat magnitude cutoff that varies with distance and produces more of a bias as the cutoff samples the sparser upper end of the luminosity function. We determine two bias functions, one for the pure *WISE* TFRs both curved and linear, and one for the *I*-band and the color-corrected *WISE* TFRs:

$$b_{\rm pure} = 0.006(\mu - 31)^{2.3} \quad (22a)$$

$$b_{cc} = 0.004(\mu - 31)^{2.3}, \quad (22b)$$

where μ represents the distance modulus of a field galaxy.

From the calibrations we generate bias-corrected distances to the calibrating clusters and derive a Hubble constant from the clusters far enough away to be in the Hubble flow ($D >$ 50 Mpc). We derive $H_0 = 72.2 \pm 1.7$ km s^{-1} Mpc^{-1} for the curved pure W1 TFR and $H_0 = 71.6 \pm 1.7$ km s^{-1} Mpc^{-1} for the curved pure W2 TFR. The color-corrected W1 and W2 TFRs give the same value of $H_0 = 73.1 \pm 1.8$ km s^{-1} Mpc^{-1}, and we get $H_0 = 74.5 \pm 1.6$ km s^{-1} Mpc^{-1} using the *I*-band TFR.

To leverage the redshift reach of SNe Ia, we measure the zero-point offset of the UNION2 SN Ia sample by comparing the distances in 56 SN Ia hosts galaxies in common with the Cosmic Flows 2 sample. The measured offsets give $H_0 = 73.7 \pm 2.4$ using the curved W1 and W2 TFRs and $H_0 = 75.9 \pm 2.5$ using the *I*-band linear TFR. Taking the log average of these values gives a Hubble constant of $H_0 = 74.4 \pm 1.4$ km s^{-1} Mpc^{-1}. The total systematic error on our measure of H_0 includes the systematic error in the calibration, the zero-point error, the SN Ia distance error, and a band-to-band systematic measured using the *I* band and W1 and W2 and amounts to ± 2.4 km s^{-1} Mpc^{-1}. Thus, our best value is $H_0 = 74.4 \pm 1.4$(stat) $\pm$ 2.4(sys) km s^{-1} Mpc^{-1}. Our estimates of H_0 do not favor the low values of H_0 presented in Collaboration et al. (2013) and Hinshaw et al. (2013), although relativistic corrections may resolve this tension as suggested in Clarkson et al. (2014).

We acknowledge useful conversations with the following people: Wendy Freedman, Barry Madore, Eric Persson, and Andrew Monson.

J.D.N. and M.S. acknowledge support from the NASA Astrophysical Data Analysis Program under grant NNX12AE19G for the *WISE* Nearby Galaxies Atlas.

H.C. and J.S. acknowledge support from the Lyon Institute of Origins under grant ANR-10-LABX-66 and from CNRS under PICS-06233. R.B.T. acknowledges support from the US National Science Foundation award AST09-08846. We acknowledge the use of the HyperLeda database (http://leda.univ-lyon1.fr).

This publication makes use of data products from the *Wide-field Infrared Survey Explorer* (*WISE*), which is a joint project of the University of California, Los Angeles, and the Jet Propulsion Laboratory/California Institute of Technology, funded by the National Aeronautics and Space Administration.

This research has made use of the NASA/IPAC Extragalactic Database (NED), which is operated by the Jet Propulsion Laboratory, California Institute of Technology, under contract with the National Aeronautics and Space Administration.

REFERENCES

Aaronson, M., Bothun, G., Mould, J., et al. 1986, ApJ, 302, 536
Ade, P. A. R., Aghanim, N., Arnaud, M., et al. 2014, A&A, 566, 54
Amanullah, R., Lidman, C., Rubin, D., et al. 2010, ApJ, 716, 712
Beers, T. C., Flynn, K., & Gebhardt, K. 1990, AJ, 100, 32
Clarkson, C., Umeh, O., Maartens, R., & Durrer, R. 2014, arXiv:1405.7860
Courtois, H. M., & Tully, R. B. 2012, ApJ, 749, 174
Courtois, H. M., Tully, R. B., Fisher, J. R., et al. 2009, AJ, 138, 1938
Courtois, H. M., Tully, R. B., & Héraudeau, P. 2011a, MNRAS, 415, 1935
Courtois, H. M., Tully, R. B., Makarov, D. I., et al. 2011b, MNRAS, 414, 2005
Fitzpatrick, E. L. 1999, PASP, 111, 63
Freedman, W. L., Madore, B. F., Scowcroft, V., et al. 2012, ApJ, 758, 24
Frei, Z., & Gunn, J. E. 1994, AJ, 108, 1476
Giovanelli, R., Haynes, M. P., Herter, T., et al. 1997, AJ, 113, 22
Giovanelli, R., Haynes, M. P., Salzer, J. J., et al. 1995, AJ, 110, 1059
Hinshaw, G., Larson, D., Komatsu, E., et al. 2013, ApJS, 208, 19
Huang, J.-S., Ashby, M. L. N., Barmby, P., et al. 2007, ApJ, 664, 840
Huchra, J. P., Macri, L. M., Masters, K. L., et al. 2012, ApJS, 199, 26
Karachentsev, I. D., Tully, R. B., Wu, P.-F., Shaya, E. J., & Dolphin, A. E. 2014, ApJ, 782, 4
Lagattuta, D. J., Mould, J. R., Staveley-Smith, L., et al. 2013, ApJ, 771, 88
Masci, F. 2013, ascl soft, 02010
Masci, F. J., & Fowler, J. W. 2009, in ASP Conf. Ser. 411, Astronomical Data Analysis Software and Systems XVIII, ed. D. A. Bohlender, D. Durand, & P. Dowler (San Francisco, CA: ASP), 67
Monson, A. J., Freedman, W. L., Madore, B. F., et al. 2012, ApJ, 759, 146
Oke, J. B., & Sandage, A. 1968, ApJ, 154, 21

Paturel, G., Petit, C., Prugniel, P., et al. 2003, A&A, 412, 45
Rizzi, L., Tully, R. B., Makarov, D., et al. 2007, ApJ, 661, 815
Sakai, S., Mould, J. R., Hughes, S. M. G., et al. 2000, ApJ, 529, 698
Schechter, P. 1976, ApJ, 203, 297
Schlafly, E. F., & Finkbeiner, D. P. 2011, ApJ, 737, 103
Schlegel, D. J., Finkbeiner, D. P., & Davis, M. 1998, ApJ, 500, 525
Scowcroft, V., Freedman, W. L., Madore, B. F., et al. 2011, ApJ, 743, 76
Scowcroft, V., Freedman, W. L., Madore, B. F., et al. 2012, ApJ, 747, 84
Sorce, J. G., Courtois, H. M., & Tully, R. B. 2012a, AJ, 144, 133
Sorce, J. G., Courtois, H. M., Tully, R. B., et al. 2013, ApJ, 765, 94
Sorce, J. G., Tully, R. B., & Courtois, H. M. 2012b, ApJL, 758, L12
Tully, R. B., & Courtois, H. M. 2012, ApJ, 749, 78
Tully, R. B., Courtois, H. M., Dolphin, A. E., et al. 2013, AJ, 146, 86
Tully, R. B., & Fisher, J. R. 1977, A&A, 54, 661
Tully, R. B., Pierce, M. J., Huang, J.-S., et al. 1998, AJ, 115, 2264
Tully, R. B., Shaya, E. J., Karachentsev, I. D., et al. 2008, ApJ, 676, 184
Tully, R. B., Verheijen, M. A. W., Pierce, M. J., Huang, J.-S., & Wainscoat, R. J. 1996, AJ, 112, 2471
Willick, J. A. 1994, ApJS, 92, 1
Wright, E. L., Eisenhardt, P. R. M., Mainzer, A. K., et al. 2010, AJ, 140, 1868